UNIVERSITY OF CALIFORNIA,
IRVINE

Ion and Particle Transport in Nanopores

DISSERTATION

submitted in partial satisfaction of the requirements
for the degree of

DOCTOR OF PHILOSOPHY

in Chemistry

by

Crystal Yang

Dissertation Committee:
Professor Zuzanna Siwy, Chair
Professor Ioan Andricioaei
Professor Craig Martens

2018

DEDICATION

To my friends and family who have supported me through this segment of my life.
A special dedication to Breakfast, a purr bucket of love.

TABLE OF CONTENTS

LIST OF FIGURES

LIST OF TABLES

ACKNOWLEDGMENTS

I would like to express my deepest gratitude to my committee chair and research advisor, Professor Zuzanna Siwy. She provided the stepping stone to launching my graduate research career, and without her generosity, intellectual insight, and guidance, I would not have handled the rigors of graduate school as gracefully, nor would I have found my future direction in life.

In addition, I would like to thank all the members of the Siwy group who I have had the opportunity to work with. Their ideas, knowledge, and laughter have impacted my graduate career in only positive ways.

Lastly, I would like to acknowledge NSF and Horizon Development, LLC. For their support and funding.

CURRICULUM VITAE

Crystal Yang

EDUCATION

University of California, Irvine — March 2018
Ph.D. in Chemistry
Ion and Particle Transport in Nanopores
Advisor: Professor Zuzanna Siwy

University of California, Davis — June 2010
B.S. in Chemical Engineering

EXPERIENCE

Graduate Student Researcher — March 2013 - March 2018
University of California, Irvine
Professor Zuzanna Siwy

Teaching Assistant — September 2012 - December 2013
University of California, Irvine

Consultant — January 2012 - September 2012
Tokyo Electron Ltd.

Post Undergraduate Researcher — June 2011 - January 2012
University of California, Irvine
Professor Reginald Penner

Undergraduate Researcher — August 2009 - March 2010
University of California, Davis
Professor Adam Moule

REU Undergraduate Researcher — June 2008 - September 2008
University of California, Los Angeles
Professor Richard Kaner

PUBLICATIONS

C. Yang, P. Hinkle, J. Menestrina, I.V. Vlassiouk, Z.S. Siwy, "Polarization of Gold in Nanopores Leads to Ion Current Rectification," *Journal of Physical Chemistry Letter*, vol 7, pp 4152 - 4158 (Oct. 2016)

Y. Qiu, C. Lin, P. Hinkle, T.S. Plett, C. Yang, J.V. Chacko, M.A. Digman, L. Yeh, J. Hsu, Z.S. Siwy, "Highly Charged Particles Cause a Larger Current BLockage in Micropores Compared to Neutral Particles," ACS Nano, vol 10, pp 8413 - 8422 (Aug. 2016)

Y. Qiu, C. Yang, P. Hinkle, I.v. Vlassiouk, Z.S. Siwy, "Anomalous Mobility of Highly Charged Particles in Pores," *Analytical Chemistry*, vol 87, pp 8517 - 8523 (July 2015)

Y. Qiu, P. Hinkle, C. Yang, H.E. Bakker, M. Schiel, H. Wang, D. Melnikov, M. Gracheva, M.E. Toimil-Molares, A. Imhof, Z.S. Siwy, "Pores with Longitudinal Irregularities Distinguish Objects by Shape," *ACS Nano*, vol 9, pp 4390 - 4397 (Mar. 2015)

A. Velasco, C. Yang, M.E. Toimil-Molares, Z.S. Siwy, P. Taborek, "Flow and Evaporation in Single Micrometer and Nanometer Scale Pipes," *Applied Physics* Letters, vol 105, pp 033101 (July 2014)

J. Menestrina, C. Yang, M. Sciel, I.V. Vlassiouk, Z.S. Siwy, "Charged Particles Modulate Local Ionic Concentrations and Cause Formation of Positive Peaks in Resistive-Pulse Based Detection," *Journal of Physical Chemistry C*, vol 118, pp 2391 - 2398 (Jan 2014)

S.K. Bux, M. Rodriguez, M.T. Yeung, C. Yang, A. Makhluf, R.G. Blair, J. Fleurial, R.B. Kaner, "Rapid Solid-State Synthesis of Nanostructured Silicon," *Chemistry of Materials*, vol 22, pp 2534 - 2540 (Mar. 2010)

ABSTRACT OF THE DISSERTATION

Ion and Particle Transport in Nanopores

By

Crystal Yang

Doctor of Philosophy in Chemistry

University of California, Irvine, 2018

Professor Zuzanna Siwy, Chair

Nanopores exhibit behaviors not seen in the micro-scale, such as ion current rectification or ion selectivity, which are useful for biotechnology, building of ionic circuits, and other fields. Nanopores in polymer films prepared by the track etched technique are useful due to the ease which one can scale from a single nanopore to 10^9 pores/cm^2. In addition, it is straightforward to control pore diameters, geometry, and pore wall chemistry. In this document, polymer membranes were used for two applications. For the first application, the undulating pore walls of single pores in a polyethylene terephthalate film were exploited to extend the resistive-pulse technique to distinguish between spherical and aspherical particles. In the resistive-pulse technique, particles are driven through the pore by an electrical potential while the ion current is continuously monitored. The particle's presence in the pore is detected as a current decrease, called a resistive-pulse. Particles which pass through pores with undulating diameters has a pulse whose shape reflects the pore topography. The pulses of spherical and aspherical particles are compared in both rough and smooth pores, and it was determined that undulating diameters are crucial to distinguishing between the two types of particles. In the second

application, polymer membranes with porosity of 10^8 pores/cm^2 are used for desalination in reverse osmosis experiments. Although the narrow opening of the conical pores are larger than the classical Debye length, it was found that with high surface charge densities, ion rejection still occurs. Ion rejection was found to further increase if the narrow opening was modified to positive charges, forming a bipolar junction on the pore wall. Lastly, single pores with diameters between 10-15 nm were drilled into 30 nm thick silicon nitride membranes to study low aspect ratio systems. While a bare silicon nitride pore exhibited no ion rectification behavior, when a gold layer is deposited at one pore opening, rectification was observed. This is due to the polarization of the gold, which generated regions of enhanced concentrations of ions in the pore, breaking the pore's electrochemical symmetry. The research demonstrates interdisciplinary character and a wide range of applications of nanopores.

INTRODUCTION

Nanopores are nano sized holes that span across a membrane which typically range from monolayers thick (0.3 nm) to microns thick [1][2]. There is quite an assortment of nanopores, but they can be broken down into two flavors: biological and synthetic. Biological nanopores are commonly protein structures embedded in a cell wall, with the critical diameter being as small as a few angstroms. Through an external stimulus such as ligand bonding or a change in the transmembrane electric potential, biological nanopores can act as responsive ion channels, which are the basis of nerve signal propagation in axons, hearing, vision, and other physiological processes [3][4]. Synthetic nanopores on the other hand, are created from a myriad of materials, including polymers, silicon nitride, glass, and 2D materials such as graphene [5][6][7][8]. Experimentalists are constantly pushing the boundaries of nanopore creation and materials. For example, it was recently shown that controlled dielectric breakdown is a quick, easy method to create a single nanopore with sub-nm precision in silicon nitride [9].

Much of the behavior seen only at the nanoscale level is attributed to the high surface area to volume ratio, in which surface interactions play a much larger role compared to environments of larger length scales. Such interactions have been exploited in biological nanopores for DNA sequencing or to study voltage gated mechanisms [10][11]. Synthetic nanopores on the other hand, have been used as biomimetics to better understand transport in biological pores, to create analogs to electric circuits (i.e. ionic circuits), and single molecule sensing[12][13][14].

Although biological pores have the advantage of being highly reproducible, at the atomic level, and have been found to function as biological sensors, diodes, and

desalination systems, they can function only when embedded in a fragile lipid bilayer [15]. Synthetic nanopores on the other hand, are structurally robust, offer greater size and shape control from sub nanometer to hundreds of nanometer resolution, and can be chemically modified. As such, track etched polymer based nanopores and mesopores are used for most of the studies in this thesis as it is a relatively cheap material, easily etched, and can be scaled from 1 to 10^9 pores/cm^2. Silicon nitride membranes are more fragile, but are used in situations where low aspect pore ratios are needed.

CHAPTER 1

Creation and Characterization of Nanopores

In the research performed within the thesis, nanopores in two types of material were created: in polymer and SiN films. The polymer membranes were made of polycarbonate (PC), polyethylene terephthalate (PET), and polyimide (Kapton), and were received from two sources: GSI Helmholtz Centre for Heavy Ion Research and the company it4ip. Both of these sources bombard polymer films with heavy ions to create latent damage tracks, which are then chemically etched in lab to create pores. The fluence of damage tracks ranged between 1 to 10^8 tracks/cm^2, and membrane examined were 12 μm thick. Such densities can be used on targets as small as 1 cm^2 foils to rolls of material that are meters long. In contrast, the SiN membranes were purchased from Structure Probe, Inc., and individual nanopores were drilled using S/TEM.

1.1 Latent Damage Tracks in Polymer Pores

The first step to creating pores in polymer membranes is to irradiate a polymer film with heavy energetic ions, which penetrate the foil, leaving damage tracks. Each heavy ion forms one damage track, which after wet chemical etching, leads to the preparation of one pore. There are two methods to perform irradiation: irradiation by fission fragments and irradiation from heavy ion accelerators [16][17][18][19]. Presently, the latter is the more popular method, which is used by our collaborators at GSI Helmholtz Centre for Heavy Ion Research in Darmstadt, Germany and it4ip in Louvain-la-Neuve, Belgium.

Irradiation by a heavy ion accelerator produces highly parallel, monoenergetic ions that create reproducible, homogeneous tracks [20]. Because heavier ions and higher energies can be used (compared to the fission method), this method can penetrate thicker targets. It is however, more expensive to use, and the particle flux is not as stable compared to fission fragments [2]. Typically, the accelerated ions have energies of a few MeV/nucleon, but higher energies can be achieved as well. GSI for example, uses energies of 10.1 and 13.0 MeV/nucleon to penetrate 50 um thick foils of polyimide with Kr and Au ions respectively, whereas it4ip uses a only a few MeV/nucleon with Xenon ions [21].

There are two theories that could explain the formation mechanism of damage tracks. Briefly, in the first theory, called the thermal spike model, it is thought that the material close to the heavy ion becomes heated and subsequently cooled down rapidly due to the small surface area. If the material is heated above its melting point, the cooled material becomes amorphous, forming a narrow cylinder of damaged material [22]. The second theory, called the ion explosion spike model, focuses on electronic processes. In this scenario, the travelling heavy ion ionizes the atoms in the target, creating positive ions in close proximity to each other. These positive ions repulse each other, and assume interstitial positions. Such movements create strain in the material leading to the formation of a damaged track, which is more susceptible to chemical etching than the bulk [23].

1.2 Etching Polymer Pores

To make pores, one must chemically attack the target material and enlarge the damage track. Formation of pores is determined by two etch rates: v_t and v_b, the etch rate

of the damage track and etch rate of the bulk material respectively. The v_t is dependent on the sensitivity of the damage track, and pores are formed if v_t is larger than v_b [24][25]. For the membranes received from GSI and it4ip, both sides of the membrane are irradiated under UV light (wavelength of 365 nm) for 1 hour in air to sensitize the damage track, and stored at room temperature in air pre- and post- UV irradiation.

The mechanism of how the damage tracks of polymer membranes etch are similar. For PET and PC, sodium hydroxide (NaOH) is used to cleave away each monomer. For the etching of PET, two NaOH molecules attack the central and secondary ester bonds of the PET monomer through alkaline hydrolysis. The two major products are ethylene glycol and the sodium salt of terephthalic acid [24]. This process leaves the carboxyl group exposed when the attack is on the central ester bond, which gives the etched polymer a negative surface charge at pH 7 or higher.

PC is also etched with NaOH, which undergoes four alkaline hydrolyses, which produces disodium salt of bisphenol A as a major product, and CO_3^{2-} and H_2O as minor products [26].

The mechanism to etch Kapton is also based on alkaline hydrolysis, but uses sodium hypochlorite (NaOCl) as the etching agent instead. In this case, the NaOCl attacks the imide bond, exposing one carboxyl group. A second attack cleaves away the main product, chlorine substituted diaminophenyl, and exposes a second carboxyl group. Presence of carboxyl groups renders the pore walls and the membrane surface negatively charged in neutral and basic solutions [21].

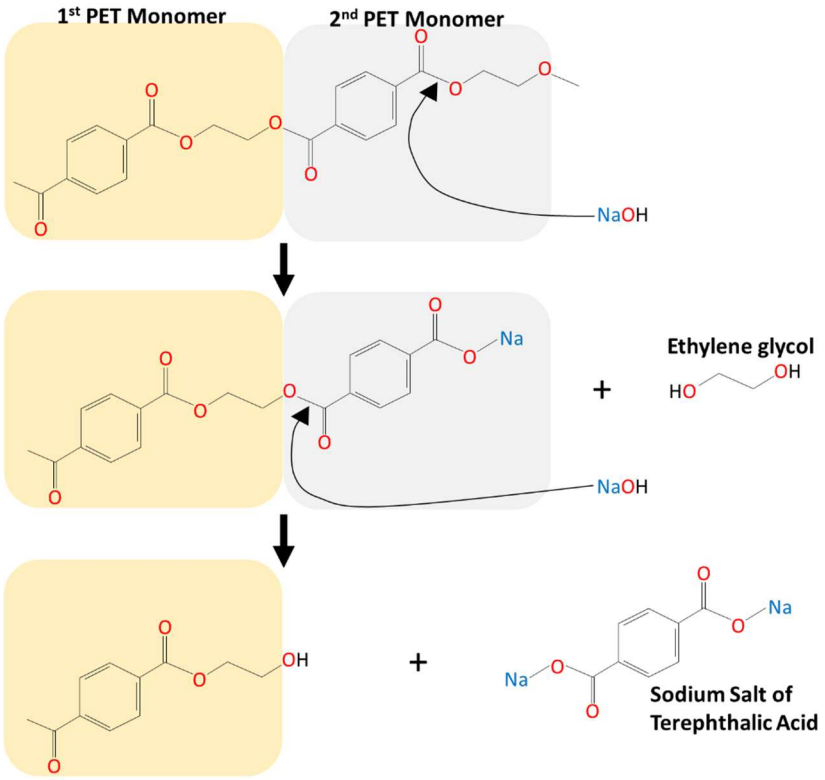

Figure 1.1 – Etch mechanism for PET. NaOH attacks the ester bonds of the PET monomer twice, exposing the carboxyl groups that give the negative surface charge at neutral pH and higher.

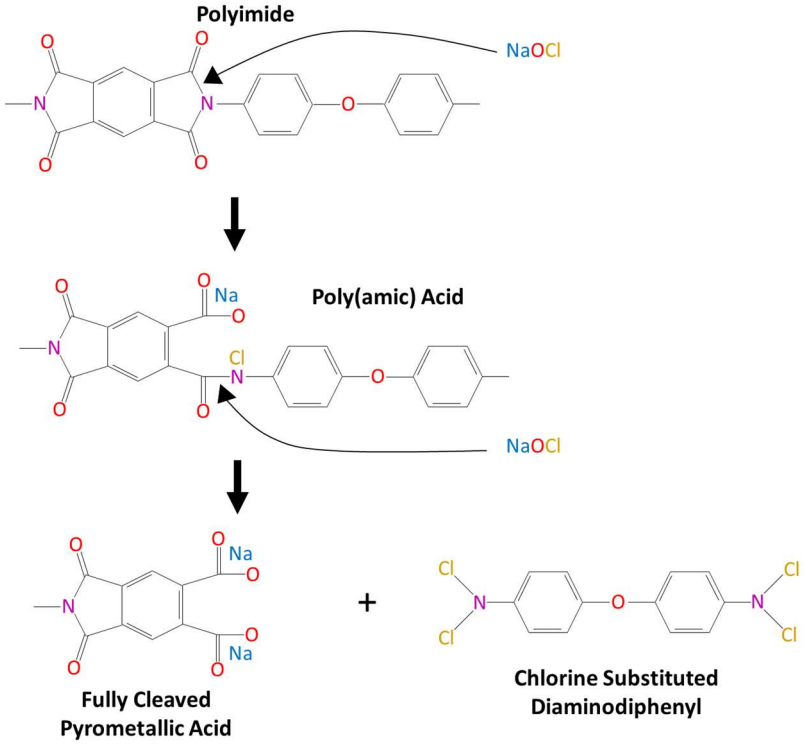

Figure 1.2 – Etch mechanism for Kapton. NaOCl attacks the imide and amine bonds, exposing carboxyl groups which have a negative surface charge at neutral pH.

Pores of various diameters and shapes can be created depending on etching conditions and the ratio between the membrane bulk etch rate to the etch rate of the track, or v_b/v_t. More explicitly, v_b controls the rate at which the pore diameter grows, whereas v_t controls how quickly the latent damage track is etched through. In the work discussed in subsequent chapters, the two most common shapes are cylindrical and conical pores, although it is possible to also create double conical and cigar-shaped pores.

To create cylindrical pores, a relatively low concentration of etchant is introduced at elevated temperatures to both sides of the membrane. In these conditions, $v_b/v_t << 1$ and the etching occurs until the etching fronts from both sides meet. The diameter of the pore will continue to enlarge until the desired pore diameter is achieved [27]. Conically shaped pores are obtained by asymmetric etching so that the etchant is placed only on one side of the irradiated foil; the other side is contact with a stopping medium, which neutralizes the etchant. In order to obtain conical pores, the v_b is still smaller than v_t but not as high compared to cylindrical pores. The side of the membrane in contact with the etchant has the large opening of a cone, called the base; the small opening, called the tip, is placed on the opposite side. Once the etchant has etched through the entire length of the membrane, the etchant reacts with the stopping solution to form a salt at the tip. In this manner, the base of the pore can continue etching while keeping the tip relatively small [28][29][2]. Figure 1.3 shows a schematic of the two etching processes leading to cylindrical and conical pores. PET, PC and Kapton pores after etching at neutral and basic pH values will have negative surface charges due to deprotonated carboxyl groups.

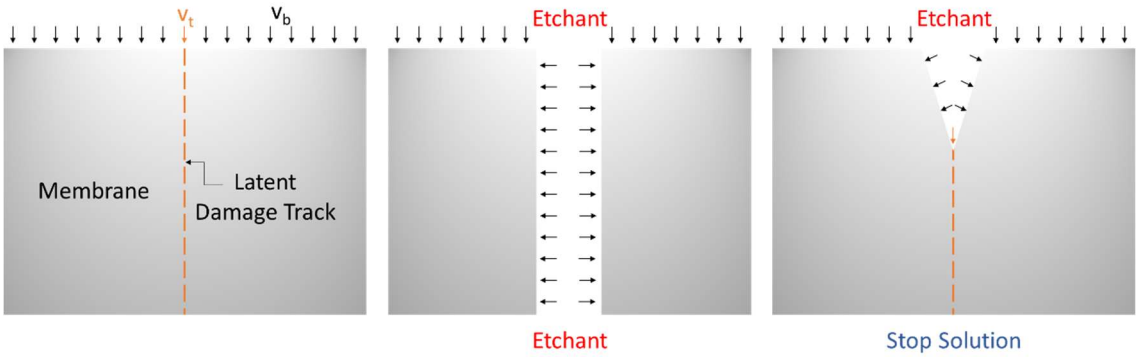

Figure 1.3 - Diagram of polymer etching processes. **A)** An unetched foil irradiated with a single heavy ion as received from GSI. Both sides of the foil are treated under UV light for 1 hour before chemical etch. **B)** Etching a cylindrical pore requires exposing both sides of the membrane to etchant at elevated temperatures so that $v_t >> v_b$. **C)** Etching a cylindrical pore requires one side of the membrane to be exposed to the etchant, and the other side a stop solution that will form a salt when the two solutions are mixed. This process generally occurs at room temperature so that $v_t > v_b$.

1.3 Drilling Nanopores through SiN

Although wet etching polymer membranes is quick, cheap, and easy to control, in single pore membranes it is not possible to image the individual pores. This is because the individual pore is located within a large area of at least 2 mm in diameter. The large area in combination with intrinsic roughness of polymers make finding the single pore using SEM impossible. Polymer pores also feature large aspect ratio, which is not always desirable. These problems may be overcome by embracing an electron microscope's propensity to damage a specimen when exposed to high electron intensity. Specifically, at high enough beam intensities (10^7 A/m^2 or greater), a beam with a spot size of a few nanometers can drill a hole through thin SiO_2 or SiN membranes [30][31]. This method has the added advantage of being able to control and measure the pore diameter in situ. Nanopores drilled in this manner have an hourglass shape, with a half-opening angle of $\sim 5^0$ [32].

1.4. Determining Pore Geometry and Size

There are several methods to determine the geometry and diameter of a single nanopore membrane. One of the most convenient ways is to record current-voltage (I-V) curve of the pore in symmetric electrolyte conditions. The slope of the I-V curve is a measure of the pore resistance, which is related with the pore geometry and size. Figure 1.4 shows schemes of the cylindrical and conical pores together with equations for their resistance.

The equations for the pore resistance can be used if we can assume that the conductivity of the solution in the pore is equal to the conductivity of the bulk solution. This assumption holds true only in solutions of high ionic strength, when the effect of the pore surface charges have a negligible effect on the number ion in the pore and on the pore conductance. For this reason, the IV curves are recorded in 1 M KCl, typically buffered with 10 mM Tris to pH 8. Under these conditions, the screening length, or so-called electrical double layer, is approximately 0.3 nm, and at low voltages is expected to have minimal effects on the IV curve.

Figure 1.5 shows an example I-V curve recorded for a single conically shaped pore in PET. The equation that relates the pore resistance with the tip opening diameter requires knowing the base diameter, which can be calculated based on the base etch rate, v_b. Base etch rate can be determined by measuring the decrease of the non-irradiated material thickness when exposed to the etchant, and is known for all polymers used in the thesis. For example, at room temperature and 9 M NaOH, the etch rate for PET is 2.13 nm/min [27]. Kapton, on the other hand, is etched at 50 ^{0}C with ~13% NaOCl and has an etch rate of 440 nm/hr [33]. For the pore shown in Figure 1.5 , which was etched for 116 minutes,

the opening diameters were found to be 10 and 500 nm assuming the pore length is equal to 12 μm.

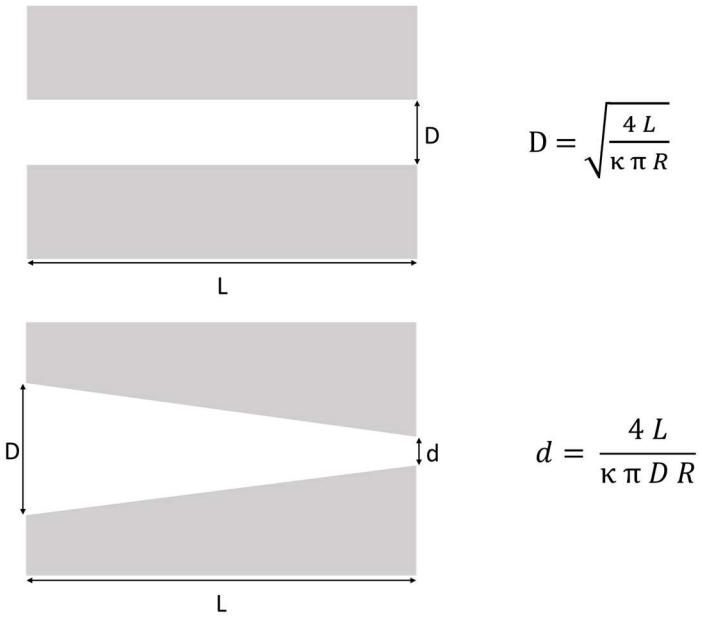

Figure 1.4 – Sizing equations for cylindrical and conical pores to determine opening diameters. The resistance, R, is determined from the slope of an IV curve. For conical pores, D is determined from the bulk etch rate [34].

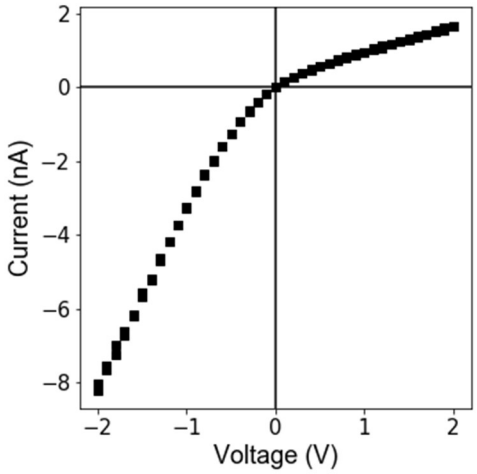

Figure 1.5 – Example I-V curve for a conical pore. The resistance is calculated from the slope of the curve, and the base diameter is calculated from the etching time and known etch rate. In this case, the I-V curve yields a pore with tip and base diameters of 10 and 500 nm respectively.

An alternate, albeit more destructive, way to determine pore size and shape is to image metal replicas of the pore. This approach however is mostly applicable to membranes containing many pores. The pores' interior is first filled with a metal via electroless deposition, and the surrounding polymer is etched away exposing the wires. The deposition conditions need to be tuned so that the pore interior is entirely filled. Figure 1.6 shows an example of the metal negative of a cylindrical pore etched from PET [35].

Determining the diameter of a nanopore in a SiN membrane is quite different compared to the method used for polymer membranes. The shape is known to be double conical in nature, with a half angle of 5 degrees [32]. Since the base diameter is measured in situ, the smallest diameter can be calculated using geometric means.

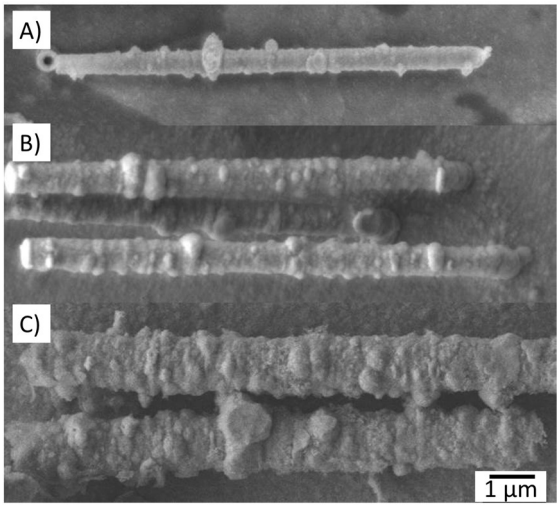

Figure 1.6 – SEM image of metal negatives of PET cylindrical nanopores. The negatives are formed by filling the nanopores with metal through electrodeposition and etching away the polymer before imaging. **A)** A 490 nm pore that was etched for 146 minutes. **B)** A 660 nm pore that etched for 186 minutes. **C)** A 1230 nm pore that was etched for 300 minutes [35].

CHAPTER 2

Transport Properties in Nanopores

Although common fluidic transport means such as diffusion and convection still apply in nanofluidic environments, complex transport behaviors arise from the higher surface area to volume ratio. Understanding the behavior of ions, analytes, and particles as they travel through nanopores are important for a range of applications, including analyte/particle characterization, ionic circuits and desalination. Before proceeding to examine the studies discussed in the next chapters, a thorough overview of transport properties is needed. This chapter will tackle the evolution and effects of the electrical double layer, as well as discuss the governing equations of nanopore transport.

2.1 Ion Transport Theory

The movement of ions occurs when a gradient is present, whether the gradient is that of temperature, pressure, electric potential, or solution concentration. In this section, the system being examined is open to atmosphere and performed at room temperature, so temperature and pressure gradients will be ignored.

Ion transport can be broken down into passive and non-passive transport. Passive transport, or diffusion in this case, is a familiar concept. When a solution has areas of high and low concentrations, the solutes in the high concentration areas will move towards the areas of low concentration to establish equilibrium. Fick's first law describes the diffusive flux of ions as it relates to concentration under steady state conditions, and reads [36]:

$$J_{Diff} = -D_i \nabla C_i \tag{2.1}$$

In one dimension, Equation 2.1 can be written as:

$$J_{Diff} = -D_i \frac{dC_i}{dx} \tag{2.2}$$

Here, J is the flux, D is the diffusion constant, C is the concentration, and the index i represents each ionic species.

The non-passive transport in the system stems from electric potential. In the experiments studied, electric potential is introduced to the system by placing two electrodes in solution and applying a voltage between them, generating an electric field. When an electric field is applied, the charged ions in the solution feels a force from the field. If the ion has a charge q in an electric field of E, assuming the ion is spherical in shape, the flux of the ions can be written as:

$$J = \frac{qEC}{\zeta} \tag{2.3}$$

Using Einstein's relation to relate the drag force, ζ, and the diffusion coefficient, $\zeta D = k_B T$, where k_B is the Boltzmann constant and T is temperature, the flux from the electric field, known as electrophoretic flux, can be rewritten as:

$$J_{EP} = D \frac{qEC}{k_B T} \tag{2.4}$$

The diffusive and electrophoretic fluxes can be combined to form the Nernst-Planck equation. Writing J_{EP} in terms of electric potential, Φ, the Nernst-Planck equation is written as [36][37]:

$$J_{i,Total} = -D_i \left(\nabla C_i + \frac{z_i e C_i}{k_B T} \nabla \Phi \right) \tag{2.5}$$

Here, z and e are the valence and elementary charges respectively. In the steady state solution, the continuity equation, $\nabla J = 0$ applies.

The electric potential can be expressed with respect to net charges of ions in the pore (existing due to the finite charge density of the pore wall) and the electric permittivity, ρ and ε respectively, using the Poisson equation [36]:

$$\nabla^2 \Phi = -\frac{\rho}{\varepsilon} \tag{2.6}$$

The combination of the Poisson and Nernst-Planck equations are known as the Poisson-Nernst-Planck equations (PNP) and are used extensively in computer modeling software such as Comsol to simulate nanopore environments.

2.2 The Electrical Double Layer

Due to the confined nature of nanopores, particles in the system interact more with the nanopore walls than they would in a system of larger length scales. These produce electrostatic interactions between the particles and the walls and is the basis of the electrical double layer.

To derive the equation for the electrical double layer, we will consider a semi-infinite planar wall, which allows us to reduce the problem to 1-dimension. The pore wall has an electric potential which is in contact with an electrolytic solution with bulk concentration, C_0. Lastly, the boundary condition is set so that the potential is 0 at an infinite distance away from the wall, and the potential is Φ_{surf} at the wall.

At equilibrium, the Poisson equation can be written as a function of concentration:

$$\nabla^2 \Phi = -\frac{\rho}{\varepsilon} = \frac{\sum_i C_i z_i F}{\varepsilon} \tag{2.7}$$

An ion near the pore surface feels the force from not only the charge on the pore wall, but also from other ions in solution. Thus, the ion distribution near the pore surface can be

expressed by the Boltzmann distribution, $C_i = C_{i0}\, e^{\frac{z_i F \Phi}{RT}}$, where C_{i0} is the ion's bulk concentration, and R is the ideal gas constant. Combining Poisson's equation with the Boltzmann distribution gives the Poisson-Boltzmann equation:

$$\nabla^2 \Phi = -\frac{1}{\varepsilon} \sum_i C_{i0} e^{-\frac{z_i F \Phi}{RT}} z_i F \tag{2.8}$$

The solution to the Poisson-Boltzmann equation gives the electric potential at some distance away from the pore wall.

When the solution has two ions of symmetric charge and the same concentration, the charge density can be written as:

$$\rho = zFC_0 \left(e^{-\frac{zF\Phi}{RT}} - e^{\frac{zF\Phi}{RT}} \right) \rightarrow \rho = -2zFC_0 \sinh\left(\frac{zF\Phi}{RT}\right) \tag{2.9}$$

When the potential is small, the sinh function can be simplified to:

$$\rho = -\frac{2z^2F^2C_0}{\varepsilon RT} \rightarrow \rho = -\frac{\Phi}{\lambda^2} \tag{2.10}$$

where $\lambda = \sqrt{\frac{\varepsilon RT}{2z^2F^2C_0}}$ is the Debye length, which gives the characteristic length scale of how far electrostatic effects exist near a charged surface in an electrolytic solution.

Recalling the boundary conditions stated above, the simplified charge density can be substituted into the Poisson equation, giving a solution of:

$$\Phi = \Phi_{surf} e^{-x} \tag{2.11}$$

where x is the distance away from the pore wall. This solution explains that the potential decreases 1/e within the Debye layer [38].

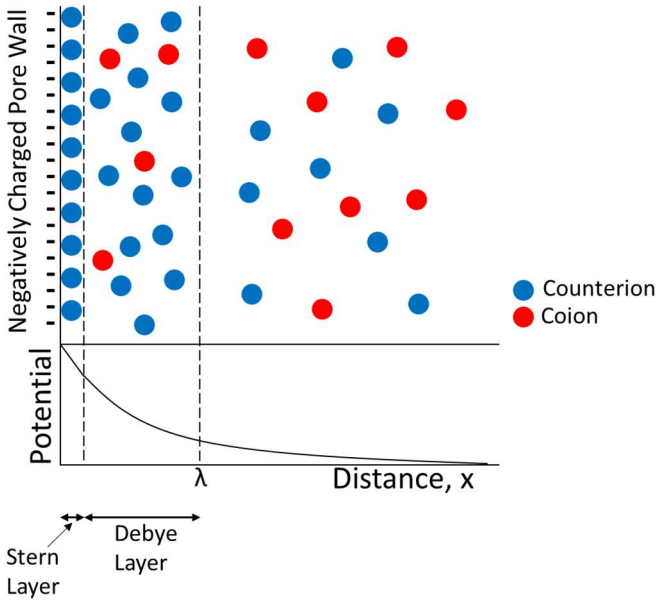

Figure 2.1 – A depiction of the Stern and Debye layers and the resulting ion distribution along a negatively charged pore wall. The behavior of the electric potential is plotted along the x axis.

Figure 2.1 shows a layer, called the Stern layer, located in between the Debye layer and the charged pore wall. This Stern layer consists of a thin layer of immobile counterions, or ions of opposite charge to the wall, and is thought to have a linear drop in potential. A closer look at the Debye layer shows most of the ions in this region also consist of mostly counterions, but are mobile. As such, the Debye length, which is inversely proportional the square root of the bulk concentration, is considered the length at which electrostatic interactions are screened. As an example, the Debye length of a 10 mM KCl solution is 3 nm, but is 0.3 nm for 1 M KCl. In narrower channels with low concentration solutions, the Debye length could span most, or even all of the channel, affecting ion/particle transport.

2.3 Transport in Conical Pores

One of the biggest factors in ion transport involves pore asymmetry, such as asymmetry in pore geometry or surface charges. For pore geometry, one can study the electric potential in a cylindrical and conical pore. In long, cylindrical pores, the concentration of counter ions in the electrical double layer is independent of the electric potential. This is seen in in a current-voltage (IV) curve, in which the curve is linear. In a conical pore, however, applying an electric potential produces an IV curve that rectifies, as seen in Figure 1.5. Here, rectification is defined as when the current at one polarity is much higher than the current at the opposite polarity. To illustrate, when the positive polarity is applied to the tip side, then the cations flow towards the base, enhancing the ion concentration, resulting in a higher current. Switching the polarity so the negative potential is applied to the tip side, the cations are now flowing towards the tip, and the anions flowing towards the base. A lack of ions, or depletion zone, is formed inside the pore, resulting in a decrease in measured current. In Figure 2.2, numerical solutions are plotted for the concentration of potassium and chloride ions along the z axis in a conical pore.

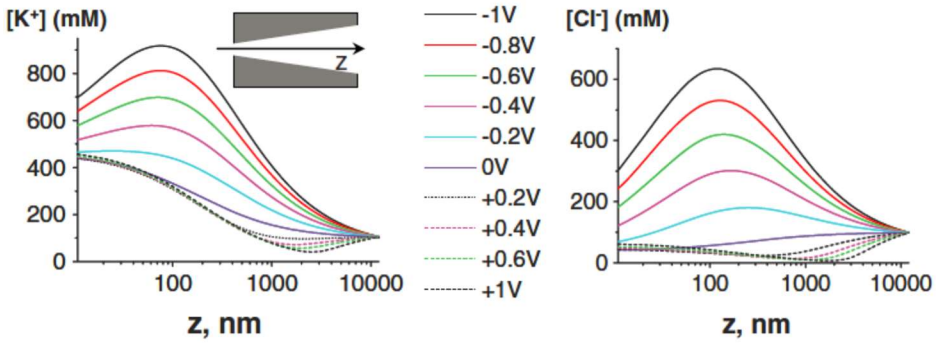

Figure 2.2 – Concentration profiles for potassium and chloride ions along the z axis for a conical pore with diameters of 5 and 500 nm at the tip and base respectively [39].

2.3 Transport in Modified Pores

Although polymer pores naturally have a negative surface charge after etching, using surface chemistry, the charges can be modified to positive charges. The specific procedure used in this laboratory to modify polymer pores utilizes EDC linking chemistry to bind amine molecules to the carboxyl groups on the pore wall, as illustrated in Figure 2.3. In the modification, 1-ethyl-3-(3-dimethlaminopropyl) carbo-diimide hydrochloride (EDC) is used. Under acidic conditions, the EDC and carboxylic acid will combine to form an o-Acylisourea intermediate. The amine molecule is now able to attach to the carboxylic group by breaking the C-O bond between the original carboxylic acid and EDC, leaving an isourea by-product. This reaction only works for primary amines, such as spermine or ethylenediamine [40].

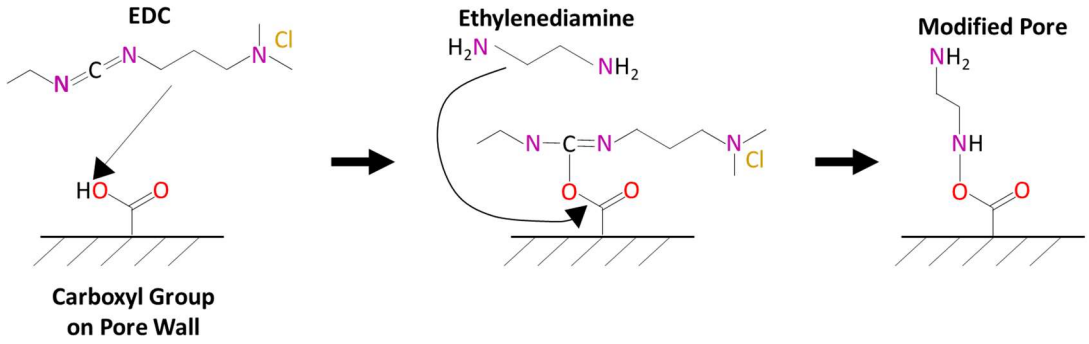

Figure 2.3 – Simplified reaction mechanism for how EDC binds primary amines to carboxyl groups.

Although the whole pore wall can be modified to positive charges, interesting transport behaviors occur when only part of the pore is modified, i.e. a boundary between positive and negative surface charge is observed. A nanopore containing such a junction is called an ionic bipolar diode. Figure 2.4 shows a cylindrical nanopore with positively and negatively charged zones. When the positive electrode is on the negatively charged side,

anions are sourced from the bulk solution from the other side of the membrane and vice versa; there is a steady stream of ions and a measurable current, known as the open state. However, when the negative electrode is on the negatively charged side, the cations inside the pore move towards the right and cannot be replenished, creating a depletion zone, creating the closed state [40]. Although Figure 2.4 illustrates open and closed states for cylindrical pores, the concept can be extended to conical pores as well. Figure 2.5 is an example IV curve for a conical PET pore. Notice that the curve is inverted compared to that of an unmodified conical pore.

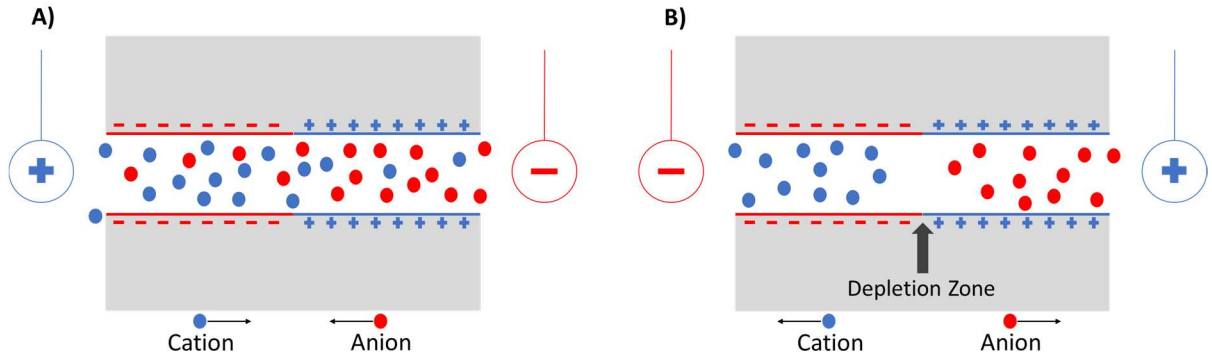

Figure 2.4 – A schematic of a cylindrical pore with positive and negatively charged zones. **A)** Ions flow continuously, creating an open state. **B)** A depletion zone is formed, creating a closed state.

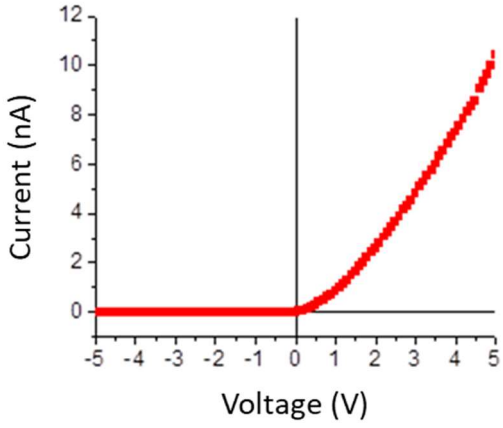

Figure 2.5 – An IV curve of a conical PET pore modified with ethylene diamine at the tip. The curve is inverted compared to an unmodified pore [41].

CHAPTER 3

Detecting Particles of Different Shapes via Resistive Pulse Sensing

The ease of fabricating pores in the nano- and micro- range has lent itself as a useful tool in resistive pulse technique, a method which has been used to detect and sequence DNA, determine particle surface charge, as well as size and count single particles. With this approach, particles as small as viruses and as big as blood cells or bacteria have been detected. In the past, the Siwy group has used polymer pores for the analysis of spherical particles and mammalian cells. This chapter details extending the resistive pulse technique to differentiate particles of similar volumes, but with different shapes with polyethylene terephthalate (PET).

3.1 – Electrokinetic Phenomena

Electrokinetics deals with the electrostatic forces that charged surfaces and particles feel when an electric field, $\vec{E}$, is applied. Recall that polymer pores have negatively charged walls, attracting cations to the surface. When an electric field is applied, the cations move towards the negative electrode, pulling liquid along with it, creating fluid flow. The fluid flow is governed by the Navier-Stokes equation [42],

$$\rho\left(\frac{\partial\vec{v}}{\partial t}+\vec{v}\bullet\nabla\vec{v}\right)=-\nabla P+\eta\nabla^2\vec{v}-\varepsilon\nabla^2\Phi\vec{E} \tag{3.1}$$

and the continuity equation, $\nabla\bullet\vec{v}=0$. Here, ρ represents the fluid density, v is the fluid velocity, P is the pressure, η is the fluid dynamic viscosity, ε is the product of ε_0 and ε_r, the absolute permittivity of vacuum and the relative permittivity of the fluid respectively, and Φ is the electric potential. After applying the continuity equation, assuming there is no

pressure gradient, and if the Debye layer is thin compared to the diameter of the pore, Equation 3.1 can be reduced to a one-dimensional form for long plane surfaces [38]:

$$\eta \frac{\partial v}{\partial y} = \varepsilon \frac{\partial \Phi}{\partial y} E_x \tag{3.2}$$

where y is normal to the x direction on a cartesian coordinate and directed into the flow, and E_x is parallel to the surface. Solving the equation using boundary conditions of $\frac{\partial v}{\partial y} = \frac{\partial \Phi}{\partial y} = 0$ as $y \to \infty$ (the edge of the diffuse layer), and $\Phi = \zeta$ (the zeta potential) when $v = 0$ gives the velocity of a particle that moves by electroosmotic flow, v_{EO} [38]:

$$v_{EO} = -\frac{\varepsilon}{\eta} \zeta_{wall} E_x \tag{3.3}$$

If a pore wall carries negative (positive) surface charges, a particle transported by electroosmotic flow will move towards the negatively (positively) biased electrode.

A more intuitive process, called the electrophoretic flow, occurs when a negatively (positively) charged particle flows towards the positive (negative) electrode. Mathematical formulations are dependent on a few assumptions about the particle: the particle is rigid, non-conducting, and has a uniform surface charge. If the Debye length is small compared to the radius of the particle, curvature effects can be ignored and the particle surface is assumed to be a local plane. Thus, the electrophoretic velocity of the particle, v_{EP}, can be derived in an analogous manner as v_{EO}, and written as [38]:

$$v_{EP} = \frac{\varepsilon}{\eta} \zeta_{particle} E \tag{3.4}$$

In nano- and micropores, electrophoretic and electroosmotic effects occur simultaneously. To determine the effective velocity of the particle, v_{eff}, the electrophoretic and electroosmotic velocities can be added together [43]:

$$v_{eff} = \frac{\varepsilon E}{\eta}\left(\zeta_{particle} - \zeta_{wall}\right) \tag{3.5}$$

The zeta potentials of the particle and the pore wall are the determining factors as to whether a particle moves in the direction of electrophoresis or in the direction of electroosmosis. Specifically, if the particle has a high (low) zeta potential compared to the zeta potential of the wall, the particle moves in the direction of by electrophoresis (electroosmosis).

3.2 – Resistive Pulse Technique

The resistive pulse technique is used to count and size particles in an electrolyte solution, such as complete blood counts in the medical setting [44]. Briefly, the technique uses a single pore that separates two electrolyte solutions. On one side of the pore, the solution contains the particles to be analyzed, and on the other side, the same solution without particles. When an electric potential difference is applied, a baseline current is established through an empty pore. When a particle passing through the pore is detected, the current deviates from the baseline current. The current deviation is generally detected as a current decrease (Figure 3.1) due to increased resistance inside the pore (i.e. the volume of the particle blocks the current), but in the case of highly charged particles, such as DNA, the current deviation manifests itself as a current increase.

For spherical particles, the relative current drop can be predicted from the following equations [45][46]:

$$\frac{R_{particle} - R_{empty}}{R_{empty}} = \frac{I_{empty} - I_{particle}}{I_{particle}} = \frac{d^3}{D^2 L} S\left(\frac{d}{D}\right) \tag{3.6}$$

$$S_{Sphere}\left(\frac{d}{D}\right) = [1 - 0.8(\frac{d}{D})]^{-1} \tag{3.7}$$

Here, R and I are the measured resistances and currents of the pore respectively. The indexes "particle" and "empty" represent the state of the pore with and without a particle. D and d are the pore and particle diameters respectively, L the length of the pore, and $S\left(\frac{d}{D}\right)$ is a correction term, called the shape factor. Note that Equation 3.4 is the shape factor for spherical particles only.

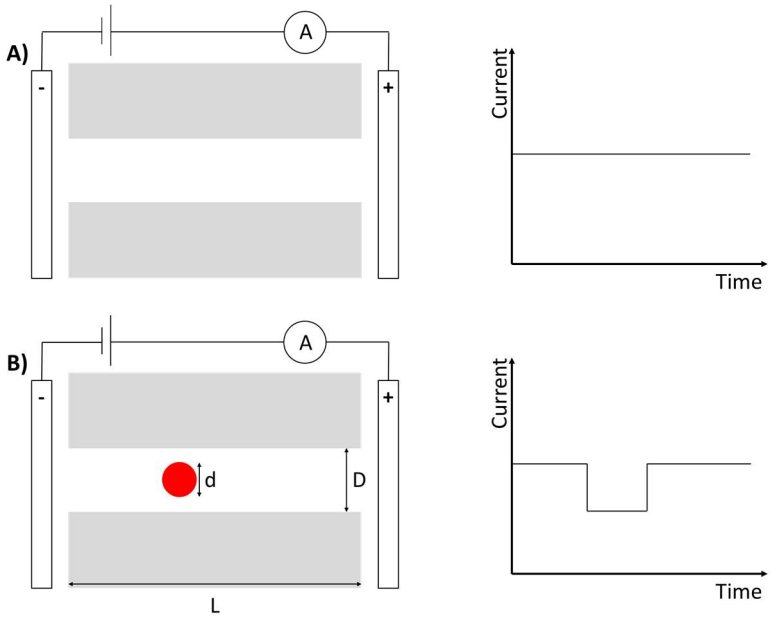

Figure 3.1 – Depiction of a pore **A)** without and **B)** with a particle, and their corresponding baseline currents. The current drops while the particle is in the pore, and returns to baseline current after the particle exits.

Figure 3.2 shows an example time series of ionic current for a PET pore of 870 nm in diameter as particles pass through the pore. The electrolyte solution was composed of 1 M KCl, pH 8, 0.1% Tween 80, and mixture of polystyrene spherical particles that were functionalized with carboxyl groups. The spherical particles were 220, 330, and 410 nm in

diameter. Each current decrease corresponds to a passage of individual particles through the pore. The depth of each current decrease correlates to the size of the particle; that is, the larger the particle, the more volume that is displaced, and the larger the current decrease.

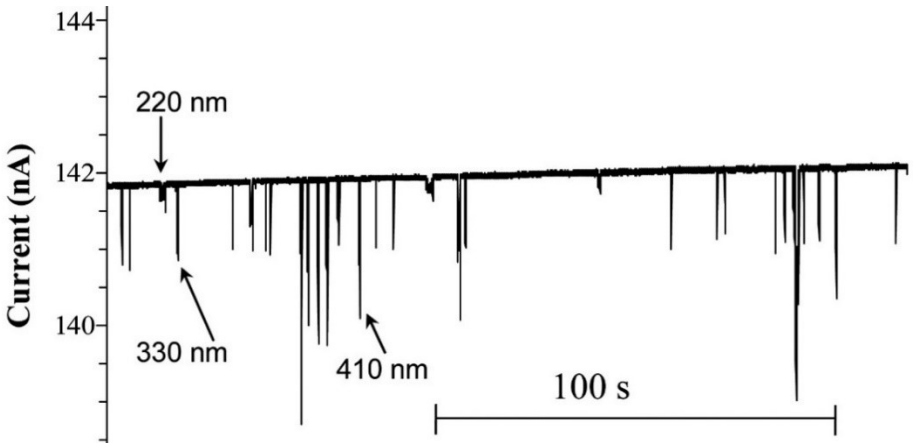

Figure 3.2– Signal of ion current versus time for a single PET pore that was 870 nm in diameter. Polystyrene particles with negatively charged carboxyl groups, of 220, 330, and 410 nm in diameter, were suspended in 1 M KCl, pH 8, 0.1% Tween 80 and passed through the pore in the direction of electrophoresis [46].

Focusing on a section where a particle translocation occurred, Figure 3.3 A depicts a single translocation event for a 410 nm particle. The event is read from left to right, which corresponds to the particle's entrance and exit from the pore. There are many localized peaks and troughs in the current, as opposed to a smooth and steady current one might expect for a smooth pore. Figure 3.3 B stacks multiple events on top of each other, vertically offset for comparison purposes. The localized peaks and troughs are mostly reproducible. Recalling that the inside of a PET pore has its own nooks and crannies, it was concluded that from the ionic current time series, one can map the topography of the inner pore walls. That is, as the particle passes through a narrower part of the pore, the current drop should be much greater than when the same particle passes through a large cavity.

Particles with different diameters show similar translocation events, but the depth of the current decreases correlates with larger particle volume [46].

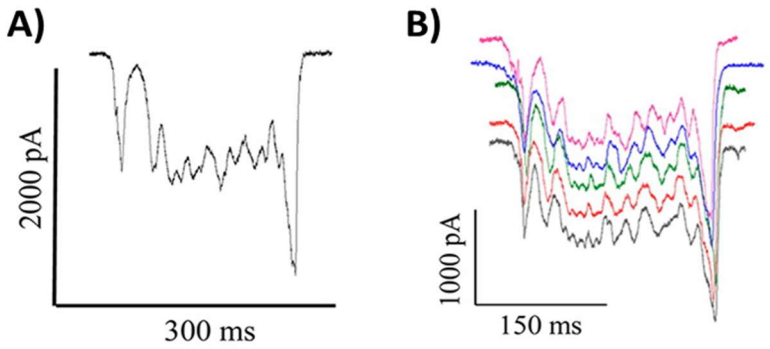

Figure 3.3 – **A)** A single translocation event for 410 nm spherical particle through an 870 nm in diameter PET pore. **B)** Multiple 410 nm spherical particles vertically offset from each other to show reproducibility [46].

The added advantage to using rough pores for the resistive pulse technique is the ease which one can detect multiple particles. If two particles are stuck together while translocating through the pore, the current decrease is doubled what is expected. In the case that a second particle enters the pore before the first particle has completely exited, the time series reveals when each particle enters and exits the pore. En_1 in Figure 3.4 shows the beginning of a current decrease, where the first particle has entered the pore. A second current decrease, En_2, shows where a second particle has entered, and the subsequent current increases, Ex_1 and Ex_2, show when the first and second particles exit the pore respectively [46].

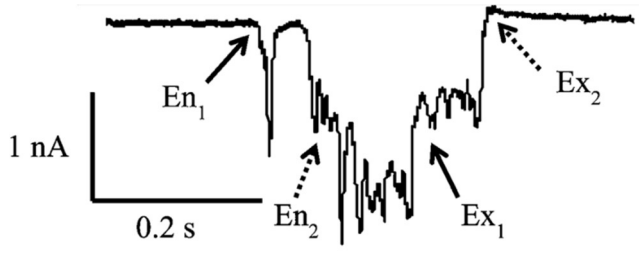

Figure 3.4 – Ionic current time series of when a particle enters the pore before the first particle has exited. The first current decrease and increase (En_1 and Ex_1) depict when the first particle has entered and exited the pore. En_2 and Ex_2 shows when the second particle entered and exited [46].

3.3 – Utilizing Pore Topography to Determine Particle Shape

In the 1973 publication, Golibersuch described resistive-pulse experiments with red blood cells passing through long single micropores. Red blood cells are known to have an oblate ellipsoidal (disk like) shape; their passage through the pore was accompanied by rotations, which caused oscillating current amplitudes. The author presented a mathematical model which predicted how the resistive-pulse amplitude depended on the cell's orientation to the pore axis [47]. However, observing oscillations requires the particle to be large, and the rotational motion to be slower compared to the translocation time. Thus, smaller aspherical particles would be indistinguishable from spherical particles of similar volume. To overcome this problem, the Siwy lab has extended the resistive pulse technique by using pores known to have rough pore walls to distinguish between spherical and aspherical particles.

The two types of particles used were polystyrene spherical beads functionalized with carboxyl groups from Bangs Laboratory, Inc., with diameters of 280 and 410 nm, and silica rods synthesized by the Imhof lab in Utrecht University. Rods with two different dimensions were studied, which will be referred to as short and long rods for the rest of the chapter. The short rods had an average length of 590 nm, and diameter of 230 nm, whereas the long rods had a much longer average length of 1950 nm, but a similar diameter of 210 nm [48]. Figure 3.5 shows TEM images of the short and long rods.

Recordings of ion current were performed with an Axopatch 200B and 1322A Digidata (Molecular Devices, Inc.). Spherical and rod shaped particles were suspended in a solution of 0.1 M KCl, pH 8, and 0.1% Tween 80. The beads, which have a surface charge of

-0.4 e/nm^2 moved in the direction of electrophoresis, whereas the silica rods, which have a lower surface charge of -0.1 e/nm^2 moved in the direction of electroosmosis.

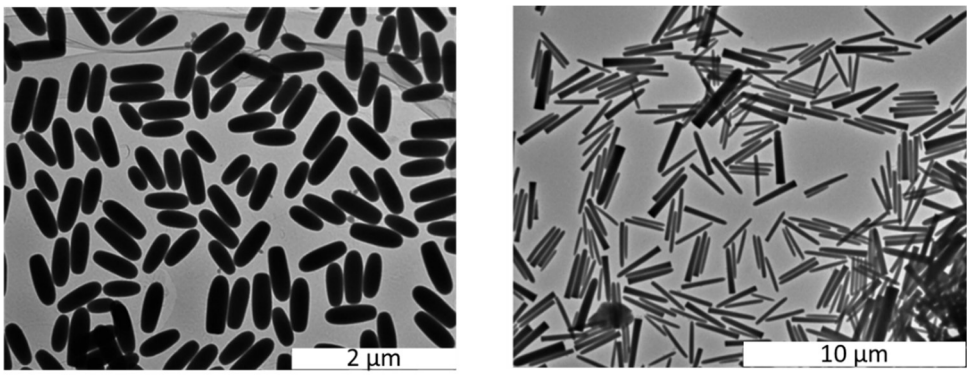

Figure 3.5 – TEM images of the silica **A)** short rods, with an average length of 590 nm and diameter of 230 nm, and **B)** long rods with average length of 1950 and diameter of 210 nm [49].

Example translocation events for a 410 nm sphere and the two rods are shown in the upper half of Figure 3.6. The particles were passed through the same side of a PET pore with average opening diameter of 770 nm and 11 µm in length. For translocation events of the spheres, the peaks and troughs are quite detailed. The contours of the ionic current time series however, became less detailed as the rod lengthened. The recordings suggest that the two rods image the pore topography with a smaller resolution than the beads. As the rods exit, there is a significant current decrease not present for the sphere, as marked by the (j) [49]. Similar current decreases were observed in previous experiments, in which negatively charged particles located at the opening on the same side as the negative electrode decreases the number of anions, resulting in a larger decrease in ionic current [50][51]. The exit effect on the sphere manifests itself as a current increase, rising above the baseline as marked by the (*). This is due to the negatively charged sphere being

located on the side of the positive electrode, increasing the number of cations, thus increasing the current [51].

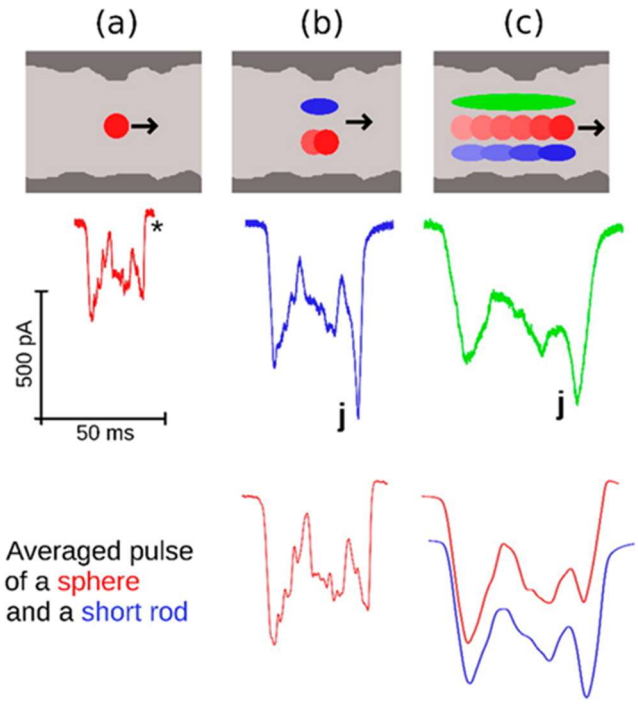

Figure 3.6 – Ionic current time series for **A)** 410 nm sphere (red), **B)** the short rod (blue), and **C)** the long rod (green) in a 770 nm diameter PET pore. The red event in A) was averaged over 11 data points to give the simulated red event in B), and averaged over 95 points to give the simulated red event in C). The blue event in B) was averaged over 148 points to give the simulated blue event in C) [49].

On the bottom half of Figure 3.6 are averaged translocation events for the sphere and short rod. The sphere has been averaged to match both the short and long rods, whereas the short rod has only been averaged to match the long rod. The averaging process using the sphere is as follows, although the process can be extended for the short rod as well. First, the number of points to average should be equivalent to the time it takes for the sphere to travel the length of the rod. This traveling time can be found by subtracting the length of the sphere from the length of the short rod, which gives 180 nm. Assuming the bead travels inside the pore at constant velocity, the particle velocity can be

found by dividing the length of the pore by the translocation time (34 ms), yielding a velocity of μm/ms; the time is calculated to be 0.56 ms. Lastly, the number of points is found by multiplying the sampling rate (20 kHz) by the traveling time, which is 11 data points. Using this averaging process, one can indirectly compare the events of spheres with known diameters to events of unknown rods to determine rod length. Note that during the averaging process for the sphere, the more pronounced current decrease seen in the rods cannot be reproduced, and the increased cationic effects at the sphere's exit remain. Thus, the entrance and exit effects are unreliable for the averaging process [49].

3.4 – Determining Particle Volume

A more quantitative approach to evaluate differences between the translocation events of spheres and rods would be to determine if the current decrease can be correlated to the particle's volume. Assuming the rods are perfect cylinders, the volume of the sphere is ~1.5 and 0.5 times the volumes of the short and long rods respectively. The average current decrease, ΔI, was calculated by integrating the event's current. The data is then expressed as the relative current change, $\Delta I/I_{particle}$. Since the exit effects of both types of particles are not intrinsic to the pore, they are not included in the calculation of ΔI

The most basic formula for calculating the current decrease is $\frac{R_{particle}-R_{empty}}{R_{empty}} = f\frac{v}{V}$, where f is the shape factor, and v and V are the volumes of the particle and pore respectively. For the beads, the basic equation is derived as Equations 3.3 and 3.4. For a 770 nm pore and 410 nm sphere, the relative current decrease is predicted to be 0.012, which is in good agreement with the experimental data, as seen in Figure 3.7. In contrast, the shape factor for the rods is more complicated, and drawn from comprehensive

demagnetization and electrical shape factor tables [52]. The current decrease for the rods is calculated as:

$$\frac{R_p - R_e}{R_e} = \left[f_{-} + \left(f_{\|} + f_{-}\right)cos^2\alpha\right]\frac{v}{V} \tag{3.8}$$

where f_{-} and $f_{\|}$ are shape factors when the field is perpendicular and parallel to the axis respectively, and α is the angle between the field and axis of revolution. The shape factors for the short rods were determined to be $f_{-} = 1.75$ and $f_{\|} = 1.17$, whereas the for the long rods, $f_{-} = 2.0$ and $f_{\|} = 1.0$ [47].

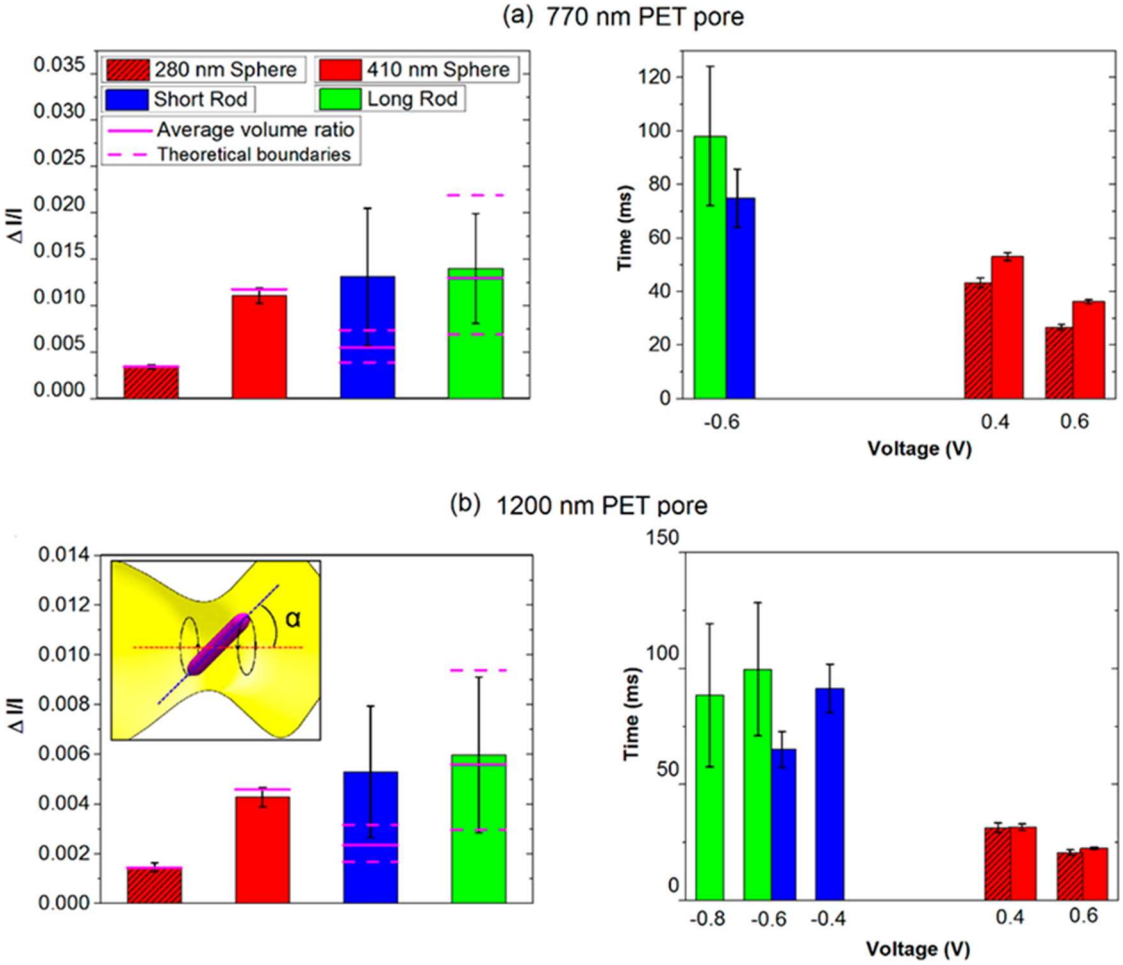

Figure 3.7 – Analysis of resistive-pulses obtained with spheres and rods in an **A)** 770 nm and **B)** 1200 nm PET pore. The pore diameters were determined by the 280 nm spheres. All particles were suspended in 100 mM KCl, pH 8 solutions. In the left panel, the relative current change is plotted for each particle. The solid magenta line is the predicted value based on Equations 3.6 and 3.8 and α = 0, whereas dotted magenta line is

the theoretical boundaries for rods of lengths and width one standard deviation above and below the average. In the right panel, the voltage vs translocation time is plotted. The inset in **B)** shows how a rod might rotate about the pore axis [49].

Using Equation 3.5 to predict the relative current decrease when $\alpha = 0$ for the short rods results in significantly lower relative current decrease than seen in the experimental data. Increasing α did not improve the fit until 90°, which is unrealistic due to steric interactions between the pore and the rod. Applying Equation 3.5 to the long rods however, showed good fit between experimental and predicted values. These trends held true for PET pores with diameters both of 770 and 1200 nm, as seen in Figure 3.7. Note that the 280 nm sphere was used to determine the diameter of the pores [49].

Surprisingly, the short rods have a higher relative current decrease than the spheres, despite having a smaller volume. This anomaly is potentially due to the rod rotating about the pore axis, displacing an effective volume in a double cone shape (see insert of Figure 3.7). The torque to induce rod rotation would be from the localized, changing electric field inside the pore due to the rough pore walls. The rotational torque, T_e, is balanced by frictional torque resisting the motion, modeled by:

$$T_e = f_r \omega \tag{3.9}$$

where ω is the rotational speed (rad/s), and f_r is the friction coefficient, calculated from the Einstein-Smoluchowski equation. The friction coefficient can be calculated from K_bT/D_{diff}, where K_b is the Botlzmann constant, T is the temperature, and D_{diff} is the rotational diffusion constant. In the 1980 publication, Tirado derives methods to calculate D_{diff}, which is calculated to be 13 and 0.8 rad/s for the rods [53]. Lastly, to approximate T_e, one can consider a 10 μm pore with regions of alternating diameters between 1000 and 1100 nm, and the length of each region being 2000 nm. As the rods travel along the pore axis, the

forces will cause the rod to move in a clockwise or counter clockwise motion. The torque applied to the rods' end can be calculated from the surface charge, electric field, and distance from the center of rotation. When 1 V is applied across the pore, ω is calculated to be around 10^4 rad/s, lending itself to the theory that the rods could be rotating quickly enough to displace a liquid volume in a double cone shape. In addition, the rod rotation is much faster than the translocation time, which is why oscillations are not observed in the translocation events [49].

3.5 – Translocation of Rods in Smooth Pores

To better understand the role of rough pore walls to distinguish between spherical and aspherical particles, as well as to better understand rod rotation, the particles were passed through polycarbonate (PC) pores, which are known to have smooth, cylindrical pores [54]. The rectangular shape of the translocation event in the right panel of Figure 3.8 also supports that PC pores are mostly cylindrical. The current decreases at the exit and entrances suggest that the pore openings are smaller than the interior of the pore. Such a phenomenon has been also been seen in the past with metal replicas and the passage of neutral PMMA particles [51]. The relative current decrease was analyzed using the current from the inside of the pore.

On the left panel of Figure 3.8, the relative current decrease has been plotted along with the theoretical average and boundaries based on Equations 3.6 and 3.8. Again, the short rods have a larger than expected relative current decrease, suggesting that the rods are performing rotation. However, the two particles have similar relative current amplitudes, suggesting that the smooth pore walls is not a conducive environment for

rotation. Overall, one can conclude that indeed, using the resistive pulse method in a pore with rough walls can distinguish between spherical and aspherical particles.

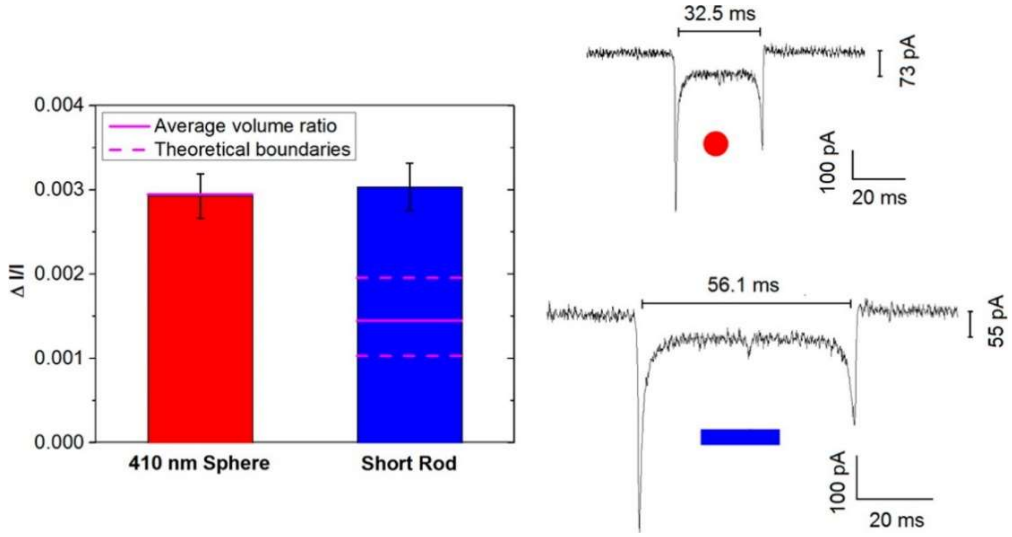

Figure 3.8 – Analysis of 410 nm sphere and short rod suspended in 100 mM KCl, pH 8 solution passing through a 930 nm PC pore. The left panel shows relative current decrease, while the right panel shows the ionic current translocations for each particle [49].

CHAPTER 4

Rectification in Polarizable Gold

Rectifying systems, which allow ion flow in one direction and hinder the flow in the opposite direction, is important to many biological functions (i.e. nerve signaling), ionic circuits, and chemical sensors. As discussed in Chapter 1, rectification comes from asymmetry in pore geometry or/and surface charge. In nanopores, some of the highest degrees of rectification are seen when a junction of positive and negative surface charge is present; such devices are called ionic diodes [41][55]. Generally, the immobile, patterned surface charges are introduced by attaching chemical groups of the desired charge to the pore surface. Creating devices with electrically addressable gates and turning charges on/off is possible, but involves complicated designs and procedures to produce multiterminal systems [13][56][57]. This chapter relays a simple way to create a two electrode system with patterned surface charges induced by an external electric field via polarization of gold. The system is versatile enough to be applied to both high and low-aspect ratio pores, of which the latter was predicted to not be able to rectify [58].

4.1 – Experimental Setup and Observations

The device is prepared by first, depositing 3 nm of chromium (Cr) as an adhesion layer onto a 50 nm thick silicon nitride (SiN) film (SPI Supplies), then an additional 12 or 27 nm layer of gold (Au) on top of the Cr. The metals are deposited with a Temescal CV-8 E-beam evaporator in a cleanroom environment. A pore is then drilled through the metal and silicon nitride layers with a FEI Titan 80-300 S/TEM at 300 kV in STEM mode. Measurements were taken with an Axopatch 200B, Digidata 1322a (Molecular Devices)

with the working electrode on the metal covered entrance, in a 3D printed PDMS conductivity cell. To decrease hydrophobicity in the pore, solutions were composed of 50% ethanol and 50% water solutions. Aqueous solutions were prepared with potassium fluoride (KF) instead of potassium chloride (KCl) because the anion, F^-, does not adsorb onto Au, allowing only the effects of induced charges to be considered [59].

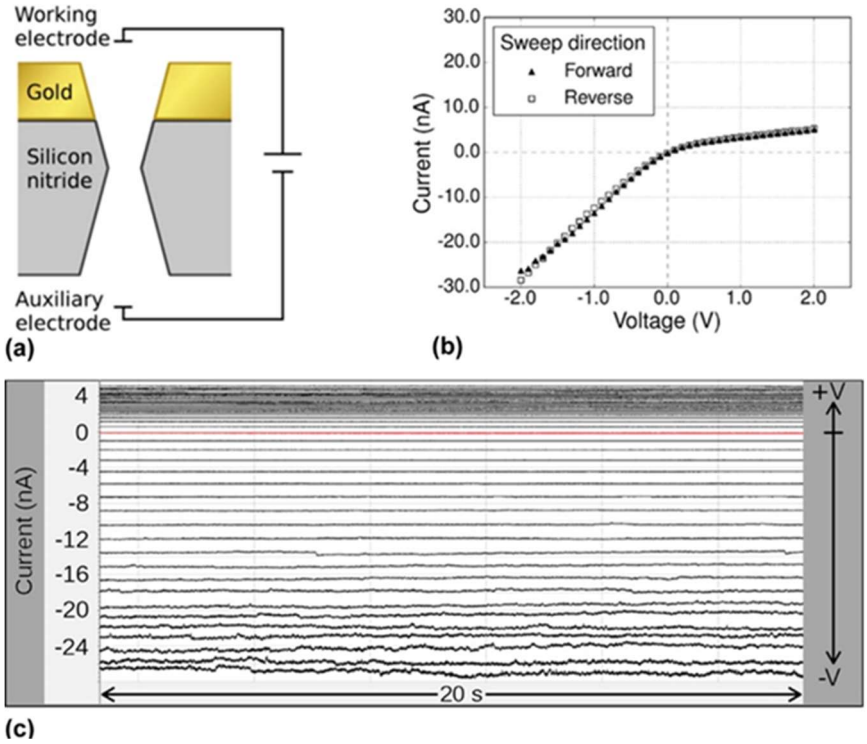

Figure 4.1 – **A)** A schematic of a single, 50 nm thick SiN nanopore with an Au layer at one opening. The working electrode is on the Au side for all experiments. **B)** An IV curve from averaging the last 0.5 seconds of the currents in panel C for a 12 nm in diameter SiN pore with 30 nm Cr, Au layer. **C)** Current signals that are 20 seconds long, for a voltage range of ± 2V in 100 mV steps [60].

An example recording of a SiN nanopore that is 12 nm in diameter is show in Figure Figure 4.1 B and C. In panel c, the ion current measurements were performed for voltages between -2 to 2 V in 100 mV steps. Each voltage was recorded for 20 seconds to ensure current signals were stable. Panel b was produced from averaging the last 0.5 seconds of each voltage in panel c. Both panels show that ionic currents were larger at negative

voltages, indicating that rectification is occurring. Further evidence of rectification is shown in Figure 4.2, where the rectification ratio, defined as the current at negative voltage over the current at positive voltage, for 100 mM KF is higher than the ratio for 500 mM KF. The rectification behavior is confirmed to be a result of the Au, since a nanopore without the metal has a rectification ratio of ~1.

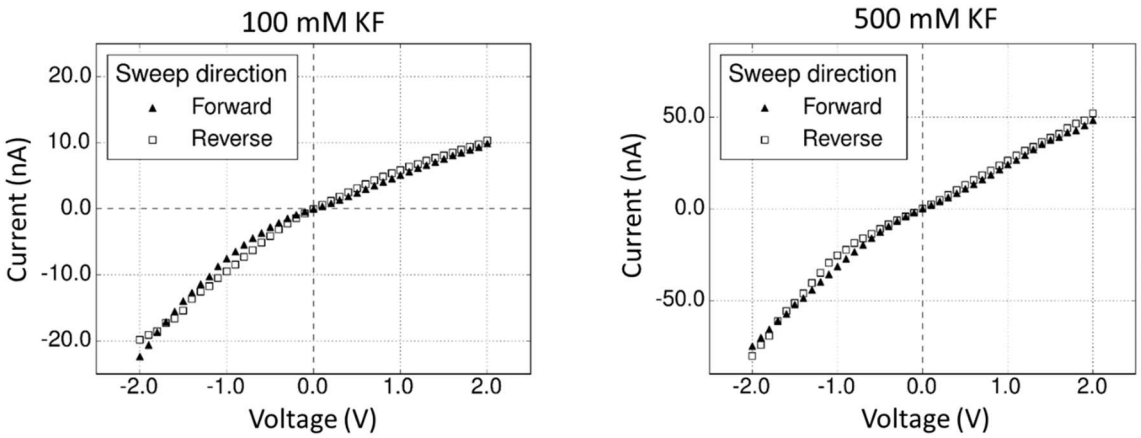

Figure 4.2 – IV curves for a pore of 9 nm diameter and 30 nm thick Au layer for (left) 100 mM KF and (right) 500 mM KF [60].

Ionic current time signals were recorded for 20 seconds because for some devices the current signal could fluctuate drastically, whether it was from wetting difficulties or gas bubble formation. An unstable signal could manifest in sudden jumps or decreases in current, making the pores seem to rectify in either direction. As such, it was impossible to separate electrokinetic phenomena from wetting problems and/or bubble formation, and pores with fluctuating currents were not included in the results. Of the 10 pores that did show stable ion currents, which had pore diameters between 9 and 16 nm, 8 of them rectified so that negative currents were higher than positive currents, one pore did not rectify, and one pore rectified so that positive currents were higher than negative currents.

4.2 – The Effects of Gold Polarization at a Nanopore Entrance

Since Au does not adsorb F^-, the effective charge on the surface of the Au should be due to the metal polarization from the transmembrane potential. The density of the induced charges on the metal surface are known to be proportional to the magnitude of the electric field [61][62]. The rectification behavior can be analyzed in two parts: 1) when the negatively biased electrode and 2) when the positively biased electrode are on the same side as the Au. Examining the former case, notice that the Au polarization makes the pore entrance effectively have a positive charge; the entrance is thus screened by an enhanced concentration of F^-. The rest of the pore has an enhanced concentration of K^+ due to the negative surface charges on both the SiN walls and the negative charge on the Au (Figure 4.3, left panel). This configuration is known as the "on" state due to both the K^+ and F^- readily sourced from bulk. In contrast, for the latter case, the surface charges on the Au and SiN pore wall creates a negative/positive/negative sandwich, similar to that of a bipolar junction transistor in a polymer pore. A depletion zone is formed, resulting in low ionic current, and is called the "off" state (Figure 4.3, right panel) [60].

To confirm that current rectification is due to Au polarization, the experiments were repeated with KCl aqueous solutions. Due to the adsorption of Cl^- on the Au layer, the effective charge on the Au layer is a superposition of the adsorbed anions and the induced charge, resulting in a reduced or even inverted rectification ratio [61]. Three different pores were introduced to 100 mM or 500 mM KF and confirmed to rectify in the direction shown in Figure 4.4. Subsequent measurements were performed in KCl of the same concentrations. In two of the pores, the rectification ratio was reduced, and the third pore had a rectification ratio of 1.

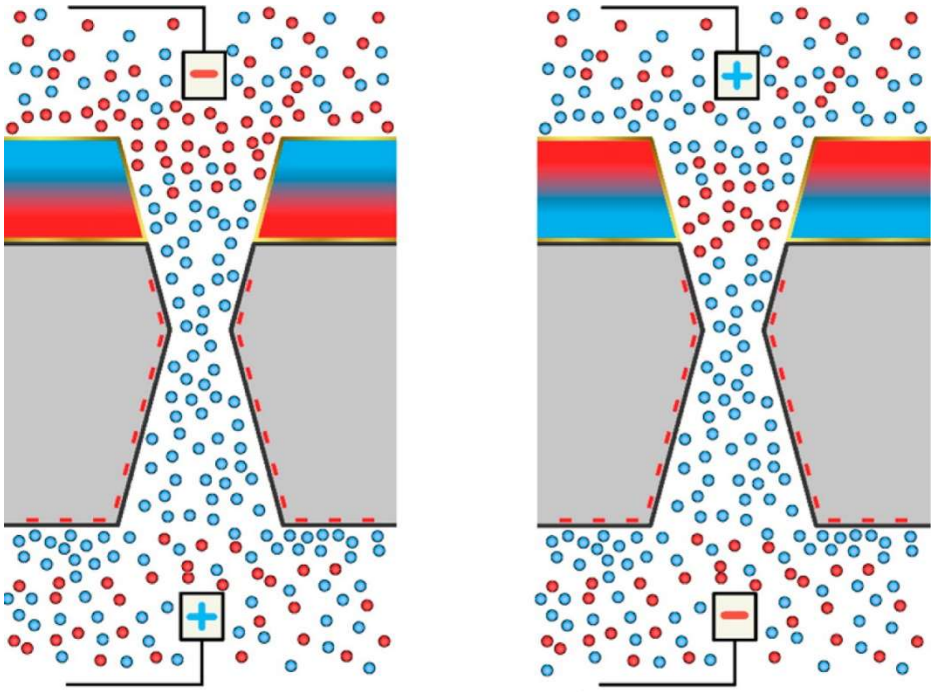

Figure 4.3 – Schematic of the surface charges and ion distribution in a SiN nanopore with an Au layer in its "on" (left panel) and "off" (right panel) states. The red (blue) strips in the Au layer indicates the induced negative (positive) charge formed by the transmembrane potential, causing a difference in ion distribution depending on the polarity of the transmembrane potential [60].

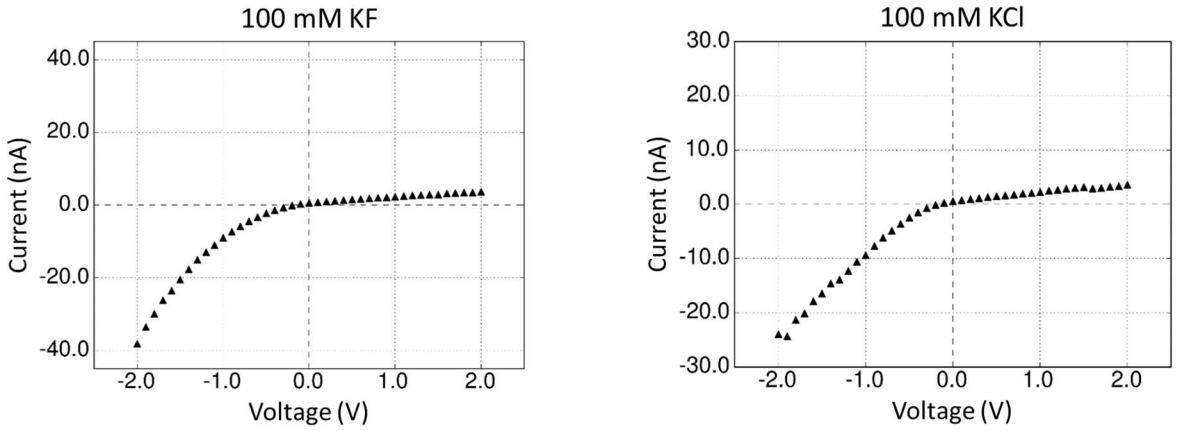

Figure 4.4 – IV curves for a SiN pore of 12 nm in diameter for (left) 100 mM KF and (right) 100 mM KCl [60].

4.3 – Electrochemical Reaction Considerations of Water and Ethanol

Electrochemical reactions have been observed in different systems that contain polarizing Au. One can determine if electrolysis of water is occurring by the equation:

$$\Delta U_{elec} = \frac{U_{tot}}{l_{cha}} l_{elec} \tag{4.1}$$

where ΔU_{elec} is the threshold at which electrolysis occurs, U_{tot} is the applied voltage, and l_{elec} and $l_{channel}$ are the length of the electrode and channel respectively. For the electrolysis of water, $\Delta U_{elec} = 1.23\ V$, while $U_{tot} = 2V$, which is the maximum applied voltage. The length of the channel is not as straight forward to calculate, since it encompasses both the length of the pore (50 nm) as well as the access resistance. The access resistance, which considers the distortion of electric field lines around the pore openings, is 0.8 times the pore diameter [63]. Thus, for a 10 nm diameter SiN nanopore, $l_{chann} = 58\ nm$. For electrolysis of water to occur, the length of the electrode must be at least ~36 nm, making it highly unlikely that electrolysis of water is occurring in this system. The electrolysis of ethanol is also calculated with Equation 4.1, in which $\Delta U_{elec} \approx 0.4\ V$, giving a minimum electrode length of ~13 nm [64]. While electrooxidation of ethanol is kinetically slow, the products from ethanol oxidation could contribute to current instability seen in some samples, thus future experiments will focus on enhancing wetting and eliminating ethanol from the solution [65][66].

4.4 – Simulated Results of Gold Polarization

The experimental findings were compared to the results from the COMSOL Multiphysics software package, in which the system was modeled by numerically solving coupled Poisson-Nernst-Plank and Navier-Stokes equations. The system modeled in shown in Figure 4.5. The double conical geometry from the SiN pore is not replicated because the rectification properties can be explained sufficiently with a diode junction inside a pore with less complex geometry.

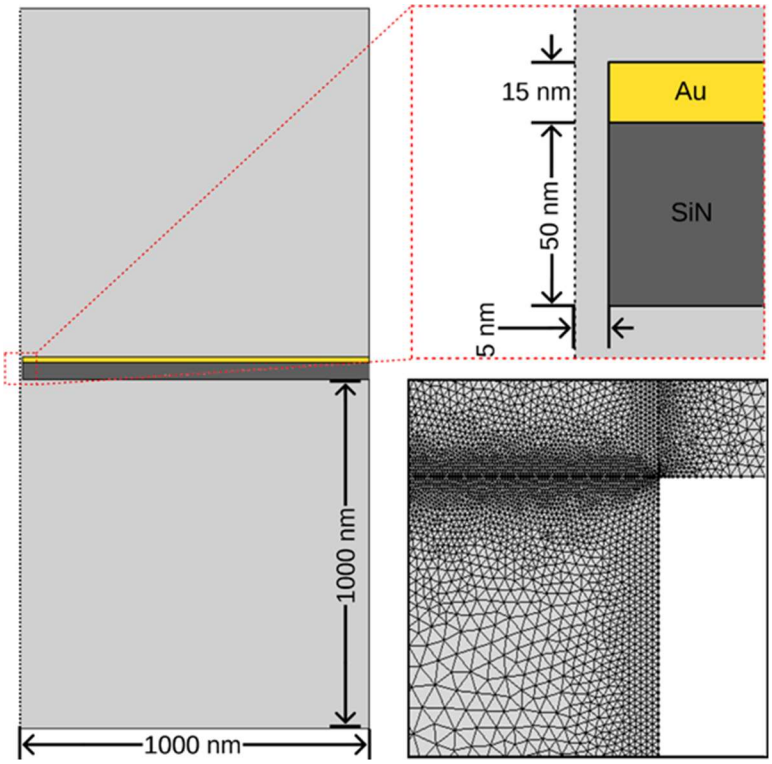

Figure 4.5 – Schematic of the nanopore model used in Comsol [60].

The basic parameters of the model is as follows. The electrodes were simulated by placing voltage boundary conditions in both reservoirs, with the working electrode on the same side as the Au layer. Boundary conditions for ion flux and pressure were placed on the reservoir walls. The Au layer was modeled by adding a 15 nm thick floating potential layer to one surface of the SiN, and a continuous surface charge of -0.016 C/m^2 is applied to the SiN pore walls to simulate native silanol charges. The bulk concentration is 100 mM, and mobilities for anions and cations are set equal to each other.

The simulated results, shown in Figure 4.6, show that the current at negative voltages are higher than those at positive voltages, and that rectification ratio is higher at lower concentrations, which agrees with the experimental findings (Figure 4.6 A). It should be noted the simulated results shown was calculated with the dielectric constant of water ($\varepsilon = 80$), but lowering the dielectric constant to $\varepsilon = 53.4$, the constant for 50%

ethanol and 50% water, only lowered the predicted currents and negative voltages by a few percent.

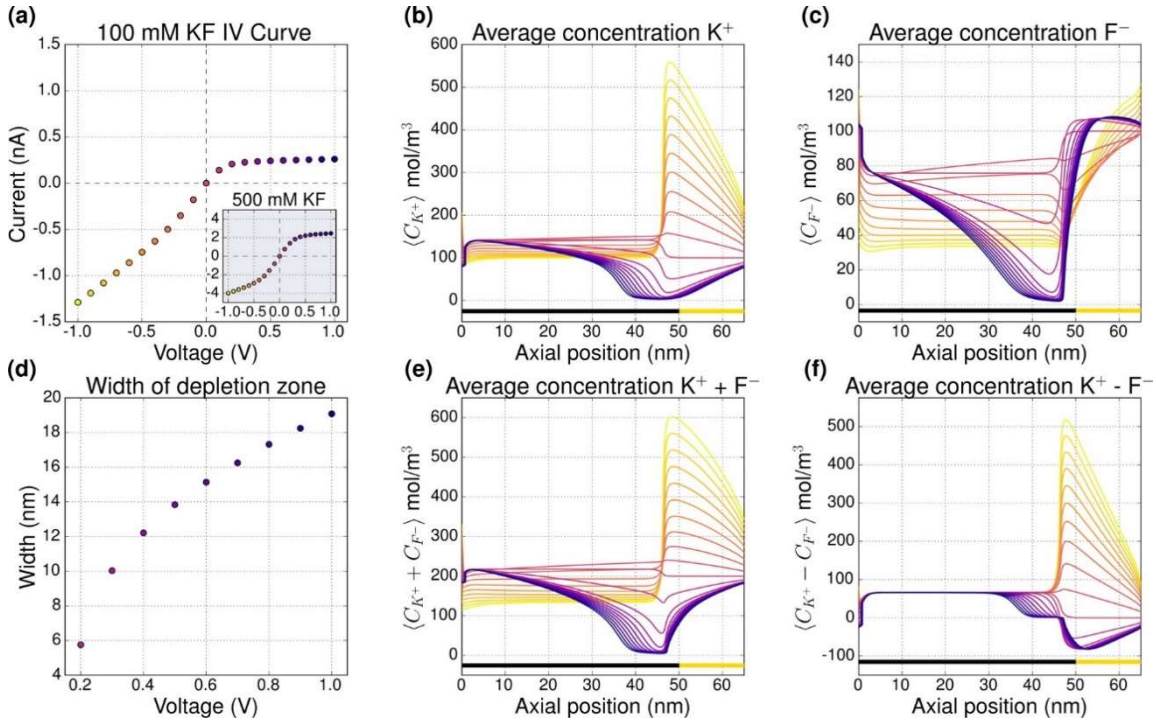

Figure 4.6 – Simulated results from solving coupled Poisson-Nernst-Plank and Navier-Stokes equations for a 50 nm thick SiN single nanopore of 10 nm diameter. An additional Au layer of 15 nm is attached to one side of the pore, indicated by the yellow line between 50 and 65 nm. **A)** IV curve for 0.1 M and 0.5 M (inset) KF. **B, C)** The average concentration of K^+ and F^- along the pore axis between -1 and 1 V. The line colors corresponds to the data point colors from panel a. **D)** The width of the depletion zone, defined as when the total ion concentration is below half the bulk value. **E, F)** The sum and difference between K^+ and F^- ions along the pore axis [60].

To determine if "on" and "off" states is seen in the model, the average concentrations of K^+, F^-, and their sums and differences along the pore axis are plotted in Figure 4.6. Looking at each ion separately, the concentration of K^+ (F^-) is enhanced at negative (positive) voltages, which is comparable to the findings of past models involving the formation of the electrical double layer due to induced charged in metals [62][61]. The averaged sums and differences of the ion concentrations reveal the presence of a bipolar junction at the SiN-Au boundary. Focusing on panel f, the averaged difference between

cations and anions, at positive voltages, there is a low ion concentration at the boundary between the two materials, resulting in low currents; this is the depletion zone described previously. Conversely, at negative voltages, there is an increase in ion concentration, exceeding bulk values, leading to enhanced currents. The width of the depletion zone is defined as the region where the average total ion concentration, panel e, is less than half of its bulk value; the results are aggregated in panel d [60].

If the same SiN-Au model is repeated with no charge on the SiN walls, the predicted IV curve has a symmetric "S-shape", confirming that the SiN's pore walls need to be charged for rectification behavior to occur. In this case, the curve behavior is due to the ionic sourcing being limited due to the nanopore's resistive element. When the positive (negative) voltage is on the Au side, the flow of anions (cations) is reduced. These results suggest that the ion rectification seen in the SiN-Au nanopore system is likely due to Au polarization.

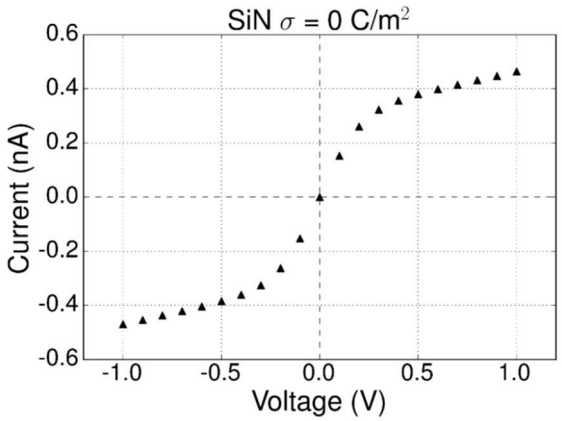

Figure 4.7 – Simulated results of an IV curve at 100 mM KF for the same system shown in Figure 4.6, except the charges on the SiN walls have been removed [60].

Using a simple, two electrode system and a metal layer at a nanopore opening, the surface charge density of a single, rectifying nanopore can be dynamically controlled. The Au layer undergoes charge polarization so that regions of the pore have enhanced or

decreased currents, depending on the polarity and magnitude of the potential. The rectification mechanism is especially applicable to low aspect ratio nanopores, and can be used in a variety of systems such as ionic switches and ionic circuits.

CHAPTER 5

Ion Rejection in Conical Nanopores with Patterned Surface Charge

Track etched polymer pores with excess surface charge showed ionic selectivity when placed in an electric field, as seen in reversal potential experiments and when current voltage curves show rectification [67][68][69]. In electric field, ion selectivity means that a pore transports preferentially cations or anions. We hypothesized that if the driving force for ion transport is exchanged for a pressure gradient, then these polymer membranes would be able to desalinate liquids via reverse osmosis. Desalination indicates that mostly water is passing through, while ions are retained on the feed side. What makes these polymer track-etched membranes suitable for reverse osmosis is that their porosity can be easily scaled up to a pore density of 10^9 pores/cm^2, surface charges patterns are easily attainable, and pore opening diameters are well controlled. The following chapter reviews the theory behind reverse osmosis and electrostatic rejections, and how they apply to simulated and experimental findings.

5.1 – Fundamentals of Reverse Osmosis

Understanding reverse osmosis requires one to first understand osmosis. In osmosis, a semipermeable membrane separates two solutions. One solution is of a pure solvent (i.e. water), and the other is a salt solution. Ideally, the two solutions want to have equal concentrations, but due to the presence of the membrane, only water molecules can travel between solutions. Thus, over time, the liquid level of the salt solution increases, while the liquid level of the pure solvent decreases by the same amount. Eventually, the flow of water reaches steady state due to hydrostatic pressure. This pressure is known as

the osmotic pressure, Π. Reverse osmosis, as the name implies, is the opposite of osmosis, in which the water from the salt solution, called the feed, is driven into the pure solvent bath, or the permeate side. For this to happen, the pressure applied must overcome the osmotic pressure [70]s.

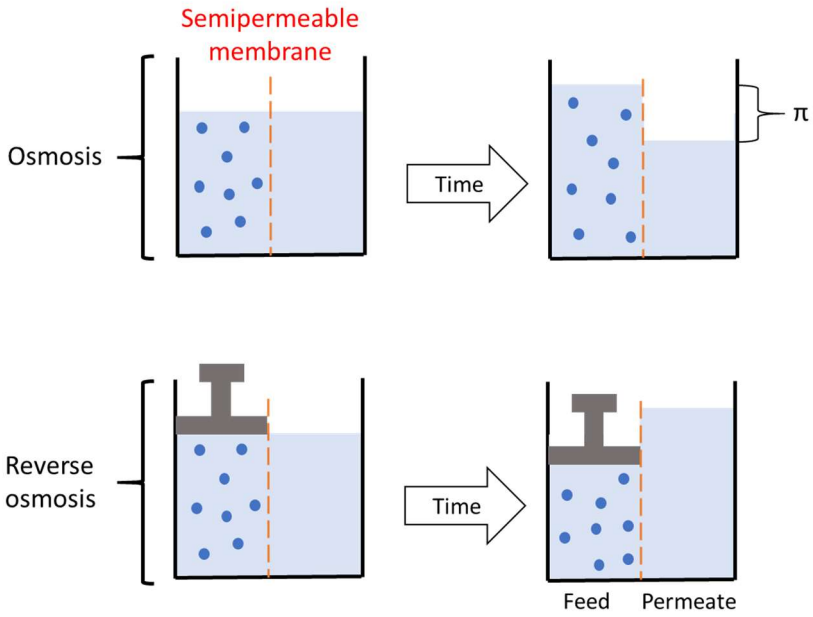

Figure 5.1– A schematic that explains osmosis (top panel) and reverse osmosis (bottom panel). With osmosis, the water diffuses across the semipermeable membrane from low to high concentration until the chemical potentials of the two solutions are equal. The osmotic pressure is the hydrostatic pressure that offsets the diffusion. In reverse osmosis, pressure is applied to the high concentration solution, forcing water into the low concentration solution. The pressure applied must be at least equal to the osmotic pressure.

From a thermodynamic standpoint, the osmotic pressure can be calculated if the compositions of the two solutions are known. The direction of flow is determined by the chemical potential, in which matter flows from high to low chemical potential. Thus, at osmotic equilibrium, the chemical potential of the solvent on both sides is the same. The chemical potential of the solute does not have the same conditions because the solute cannot pass through the membrane. The chemical potential of a species, μ_i, is written as:

$$\mu_i = \mu_i^0 + RT \ln a_i \tag{5.1}$$

where μ_i^0 is the standard chemical potential for species i at temperature T, R is the gas constant, and a_i is the activity. The activity is generally equal to the ratio of the vapor pressure above the solution to the vapor pressure above the pure solvent. When the solution is dilute, Raoult's law can be applied, so that $a_i = \frac{P_i}{P_i^0} = x_i$, where P is the vapor pressure, and x_i is the mole fraction of the species. At constant temperature, the chemical potential depends on the pressure and composition of the solutions. When at equilibrium, no flow is occurring, or $d\mu_i = 0$, then the total derivative of the chemical potential becomes:

$$\left(\frac{\partial \mu_i}{\partial P}\right)_{T,x_i} dP = -\left(\frac{\partial \mu}{\partial x_i}\right)_{T,P} dx_i \tag{5.2}$$

Using partial derivations and substitutions from Gibb's free energy equations, Equation 5.2 can be transformed into:

$$\int_{P_0}^{P_0+\Pi} v_i \, dP = RT \int_0^{x_i} \frac{dx_i}{1-x_i} \quad \rightarrow \quad \Pi v_i = -RT \ln(1-x_i) \tag{5.3}$$

Since the solution assumed to be dilute, Raoult's law can be invoked again, so that $\ln(1-x_i) = -x_i \cong \frac{N_i}{N_s}$, where N represents the moles of the species i and solvent s. With a little more simplifications and substitutions, the more conventional form of osmotic pressure, known as van't Hoff's Equation, can be written [71]:

$$\Pi = iC_iRT \tag{5.4}$$

where C_i is the molar concentration of the species, and the variable i is the Van't Hoff factor. This factor is the ratio between the measured concentration of particles after dissolution and the calculated concentration based on mass. Most non-electrolytes have a

Van't Hoff factor of 1, but for ionic compounds, the factor is equal to the number of ions dissolved. For example, the Van't Hoff factor for KCl is 2, and 3 for $CaCl_2$.

5.2 - Electrostatic Rejection

Most traditional RO membranes reject ions through steric impedance. In other words, they reject ions based on size exclusion. For K^+ and Cl^-, the diameter of the first solvation shell in aqueous solutions is ~6.7 Å and 6.4 Å respectively, so for perfect rejection, pores must be smaller than these diameters [72][73]. An alternative approach for salt rejection is to use electrostatic rejection, a method that the polymer membranes can capitalize upon due to its charged pore walls when in contact with electrolytic solutions. To understand the mechanism of electrostatic rejection, imagine a system similar to Figure 5.2 A. Recall that at low ionic concentrations, the Debye layer is relatively large, and filled with counterions. As the pressure is applied to the feed side, water is pushed through the pore, moving parts of the Debye layer with it, and allowing counterions to exit the pore. To not violate electroneutrality principles in the permeate solution, any exiting counterions must be accompanied by an exiting co-ion. However, the low number of co-ions in the pore compared to bulk concentrations makes it difficult for ions to exit, thus, ions are unable to exit the pore.

While the above describes the mechanism for how a homogeneously charged nanopore reject ions electrostatically, there is evidence that the rejection rate will increase in inhomogeneously charged nanopores [74][75][76][77]. The mechanism for ion rejection in an inhomogeneously charged nanopore is similar to that of a homogeneous system. Take for example, a system such as Figure 5.2 B, in which the nanopore has

negatively charged walls for the upper half, and a distinct boundary where the walls become positively charged in the lower half. The feed is in contact with the negatively charged portion, whereas the permeate is in contact with the positive side. Again, at equilibrium, the two regions of the pore are filled with their appropriate counterions. When pressure is applied, if an ion exits the pore, it must exit as an anion/cation pair. However, electroneutrality principles must also be observed in the interior of the pore. Replacing the cation in the negative region is a simple matter of sourcing from the feed solution. For the anion to reach the positive region, however, the anion must enter and travel through the negative region, an unfavorable situation.

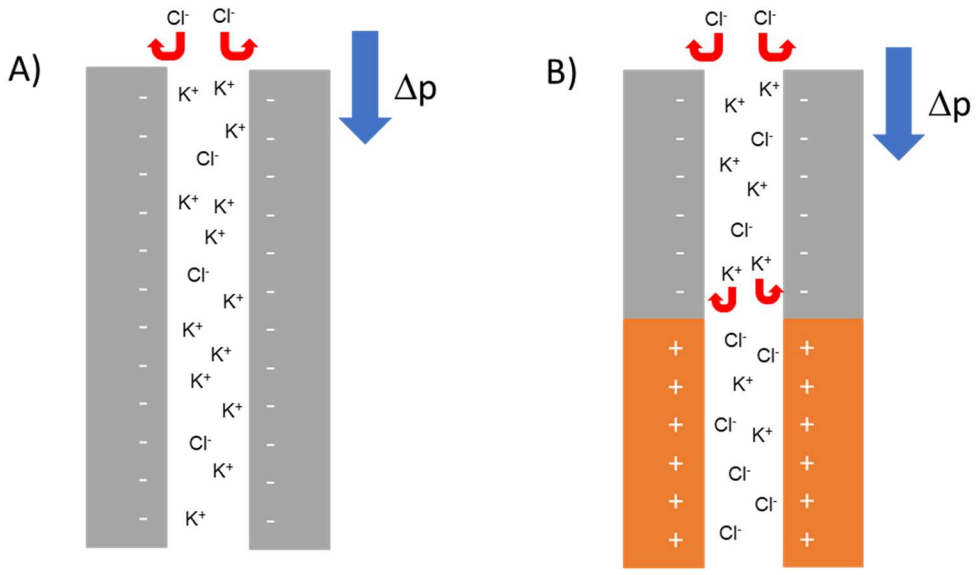

Figure 5.2 – Mechanism for electrostatic ion rejection for **A)** homogenously and **B)** inhomogenously charged walls, in which the pore is in contact with aqueous KCl. As pressure is applied, water flows from the top to the bottom. The interior of the pore is filled with counterions as appropriate. For a counterion to exit the pore in A), a coion must also exit due to electroneutrality requirements in the permeate. Pore electroneutrality is replenished by the feed. In **B**) however, when a pair of ions exits the pore, the pore electroneutrality is reestablished by sourcing ions from the permeate.

Similar to the formulism in Chapters 2 and 3, the coupled Poisson-Nernst-Planck and Navier-Stokes equations are used to describe ion transport through nanopores under

pressure. Compared to Equation 2.5, the extended Nernst-Planck equation has an additional term to account for convection generated by the pressure difference across the nanopore [75]:

$$j_i = -K_{i,d} D_i \nabla C_i - \frac{F K_{i,d} z_i D_i C_i}{RT} \nabla \Phi + K_{i,c} C_i v \tag{5.5}$$

where j_i is the molar flux of each species i, D_i, R, F are the diffusion constant, ideal gas constant, and Faraday's constant respectively, C_i is the concentration, z_i is the valence charge, T is the temperature, and u is the velocity of the fluid. The electric potential, Φ, is governed by Poisson's equation. Lastly, $K_{i,d}$ and $K_{i,c}$ are the hindrance factors for diffusion and convection respectively. They are functions of the ratio between the solute radius (Stokes radius) and pore radius [78][79].

The Navier-Stokes Equation also has an additional term to account for an electric component:

$$-\nabla P + \eta \nabla^2 v - F \sum_i c_i z_i \nabla \Phi = 0 \tag{5.6}$$

where P is the hydrostatic pressure and η is the fluid viscosity. The coupled PNP and NS equations are known as the space charge model, which describes a two dimensional transport system through a nanopore. It is computationally intensive to solve the coupled equations, so an approximate model, called the homogeneous approximation, can be substituted if the electrical double layer overlaps. Using the homogeneous approximation, all the terms in the extended NP equations are defined using their radially averaged quantities, and the following boundary conditions are defined [78]:

$$c_i^P = C_i^P \varphi_i e^{-z_i \Delta \Psi_D^P} \tag{5.7}$$

$$c_i^F = C_i^F \varphi_i e^{-z_i \Delta \Psi_D^F} \tag{5.8}$$

Here, the superscripts P and F represent the permeate and feed sides respectively, c_i is the concentration right inside the pore, C_i is the concentration just outside the pore, φ_i is the steric partitioning coefficient, and $\Delta\Psi_D$ is the dimensionless Donnan potential at the interface of the nanopore and bulk solution. The homogeneous approximation can be solved iteratively to produce the theoretical rejection rate, R_i, of each species [75][78]:

$$R_i = 1 - \frac{C_i^P}{C_i^F} \tag{5.9}$$

Given that these polymer pores are selective to cations due to its negative pore walls, if they could also reject anions at an appreciable amount, then multi-pored membranes could serve as a viable device for desalination by electrostatic repulsion. In addition, if the membranes can achieve salt rejection with larger than average diameters, the applied pressure needed should be lower, reducing energy costs.

5.3 – Modeling Ion Rejection with Bipolar Membranes

Much of the previous literature use nanopore systems in which the Debye length is on the same scale as the nanopore opening. Using Comsol Multiphysics 4.4 package, it was determined by us that in highly charged nanopores, salt rejection occurred even if the Debye length was smaller than the pore radius. Two types of nanopores were modeled: a conical and cylindrical, as seen in Figure 5.3. The conical nanopore has a tip and base diameter of 3 and 500 nm respectively, and is 11 μm long, while the cylindrical pore has a diameter of 10 nm and is 1 μm in length. Modeling for a range of tip and base openings was performed as well. The bottom reservoir contains the concentrated solution, while the top

reservoir is pure solvent. Pressure is applied from the bottom to the top, and ion transport follows coupled Poisson-Nernst-Planck and Navier-Stokes equations.

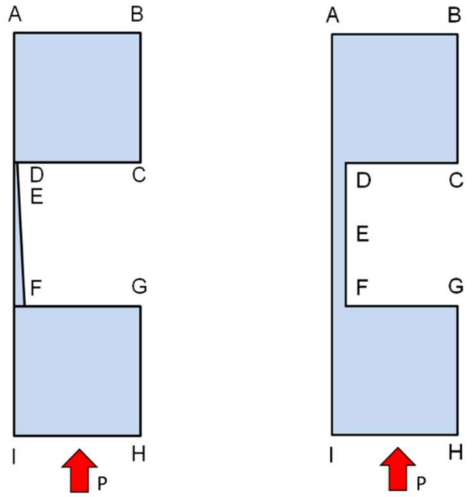

Figure 5.3 – Two types of systems used for modeling coupled Poisson-Nernst-Planck and Navier-Stokes equations with pressure: conical (left) and cylindrical (right) nanopores. For the conical system, the tip and base diameters are 3 and 500 nm respectively, with a pore length of 11 μm; a range of tip openings between 2 and 10 nm, and base openings between 300 nm and 1000 nm were considered in some simulations as well. For the cylindrical nanopore, the pore diameter is 10 nm, with a pore length of 1 μm. Pressure is applied from the bottom [80].

Using the cylindrical model as a basis, the rejection ratio as a function of surface charge of the pore wall was graphed at three concentrations: 50, 100, and 500 mM at 30 atm (Figure 5.4, left panel). The pore has a bipolar surface charge pattern with a sharp junction between the positive and negative regions that were each 0.5 μm long. Both zones had the same absolute charge density. Much of the mechanisms formulated in the previous section assumed that the Debye layer was similar in length to the pore radius and the pore wall was weakly charged. Thus, for 500 mM of 1:1 electrolyte, a Debye length of 0.4 nm constitutes only ~ 8% of the pore radius (5 nm), and at surface charge densities less than 0.05 C/m^2, salt rejection is not expected. At 50 mM solution however, the Debye length reaches ~1.4 nm, thus a 5 nm nanopore is expected to provide some salt rejection. Notice that as the surface charge densities of both regions increase, so does salt rejection. What is

remarkable is that at higher surface charge densities, salt rejection occurs even for 500 mM.

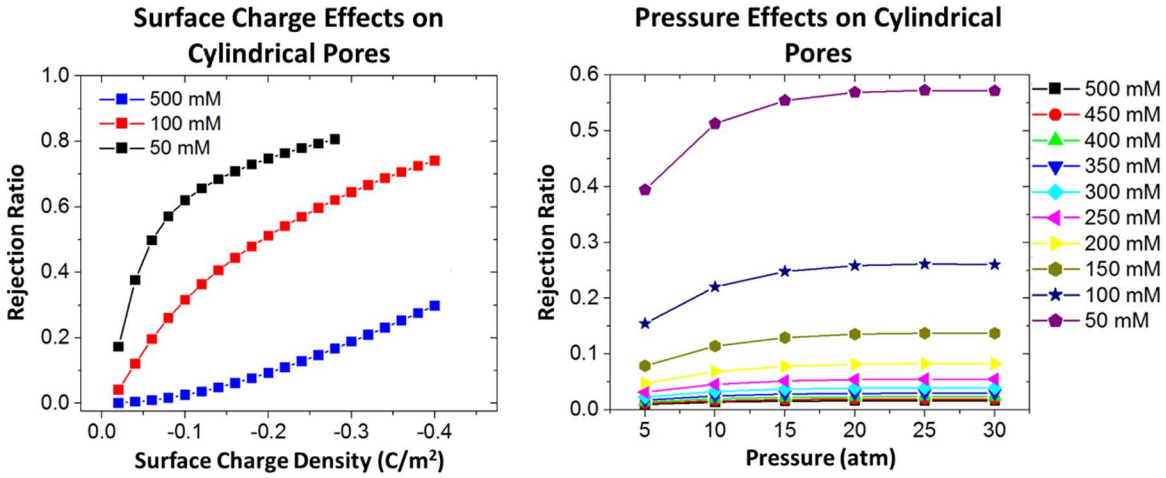

Figure 5.4 – Simulated dependence of salt rejection on surface charge density of the pore wall (left) and applied pressure difference (right) for a cylindrical nanopore that was 10 nm in diameter and 1 μm in length. The cylindrical pore has a sharp boundary between its positive and negative surface charges, 0.5 μm long each. Note that the Debye length is much smaller than the radius of the pore, but salt rejection still occurs at high surface charge densities [80].

Salt rejection generally increases with pressure due to more water being pushed through the pore and diluting the permeate solution [81]. However, Figure 5.4 (right panel) shows there is a limit to the maximum rejection. Other theoretical models show the rejection ratio decreasing ~10% from the max with higher pressure [75]. This maximum is caused by the accumulation of rejected ions near the surface of the membrane, called concentration polarization. The rejected ions can be visualized as a stagnant layer, whose thickness can be minimized with stirring. While the stagnant layer accumulates rejected ions, some of these ions diffuse back into the bulk. However, with increased pressure, the stagnant layer builds until the ion diffusion is unable to keep the concentration near the membrane surface close to bulk concentration [74].

A crucial aspect of this project, however, comes from the combination of high surface charge density, the ability to easily tune pore opening diameters, and the length of positive region in a conical pore. A conical system was modeled (Figure 5.5), in which the positive region had a surface charge density of 0.08 C/m^2 placed at the tip, and the negative region had a surface charge density of -0.08 C/m^2. All plots were created for 15 atm of applied pressure difference and 100 mM of KCl on the feed side. To understand the role of the tip opening diameter for salt rejection, we looked at the salt rejection for a set of tip openings while keeping the base opening at 500 nm. As expected, a significant decrease of salt rejection was observed when the tip opening diameter exceeded 5 nm; at 10 nm the pore basically did not reject any salt. The decrease in salt rejection with the increase of the tip openings can be easily understood when considering the Debye length versus pore opening. We also probed the importance of the base opening for salt rejection. While keeping the tip at 3 nm, the base was changed between 300 nm and 1000 nm. The pore was predicted to feature lower salt rejection for base diameters that exceeded 600 nm. We believe the modeling points to the role of the cone opening diameter on the effective area of the pore wall, which participates in rejection. If an opening angle of the cone is large (i.e. large base diameter), the local pore radius along the pore length increases quickly, diminishing the area with small enough opening, which assures salt rejection. It should be noted that although the upper two plots seem to indicate the existence of a maximum, we believe that the small changes in the salt rejection for the smallest tip and base diameters considered, might not significant and in these regimes the rejection could be considered constant.

Finally, the critical parameter, which we considered was the length of the positive zone. Intuitively, we predicted that if this zone was too long or too short, the bipolar junction ceases to be as useful, and the pore would exhibit behavior characteristics of a pore with homogenous surface charge. With a tip and base diameters of 3 and 500 nm, respectively, the optimal length of the positive region, assuring the highest salt rejection, is 25 nm. The optimal length of the positive region, however, still depends greatly on the pore's opening angle, represented here by the tip and base diameters. As an example, in panel D, the tip size is kept at 3 nm, while the base diameter varies at 250, 500, and 1000 nm. The optimal length of the positive region decreases as the base diameter increases.

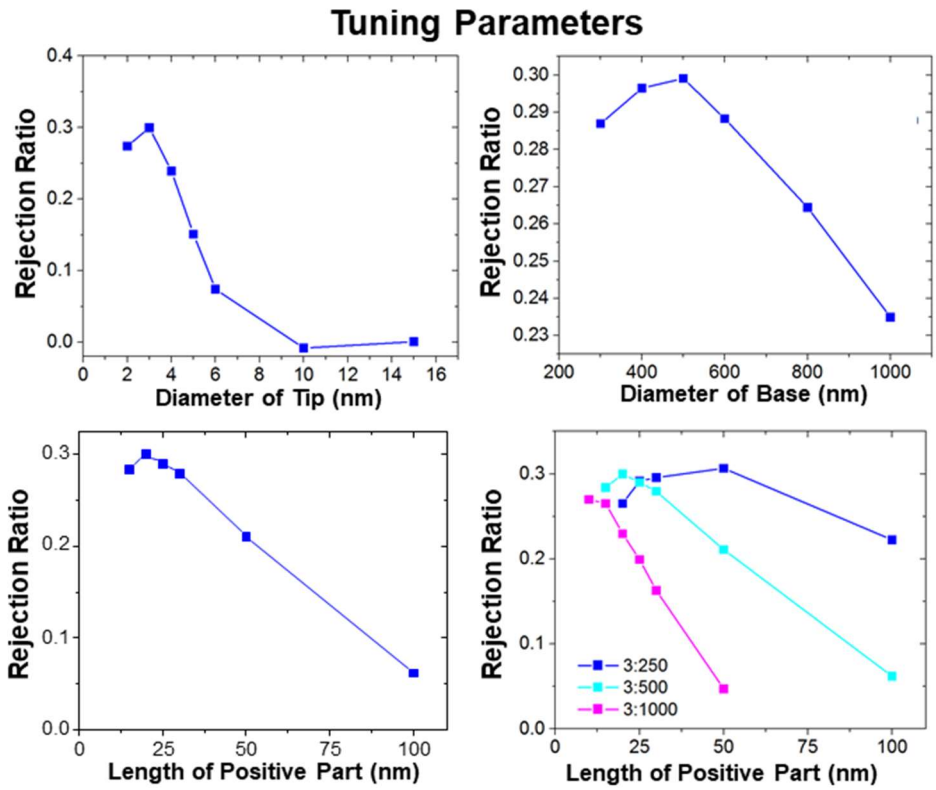

Figure 5.5 – Simulated results of salt rejection for a conical nanopore, with surface charge density of 0.08 C/m^2 at the tip side, in 15 atm and 0.1 M. The role of **A)** tip and **B)** base diameters for salt rejection was probed keeping the base and tip diameters constant, respectively. In **A** the base diameter was 500 nm, in **B** the tip was 3 nm. **C)** For a pore with openings of 3 nm and 500 nm, the optimal length of the positively charged zone was found to be 25 nm. **D)** The optimal length of the pore opening is dependent on the tip and base diameters. In this plot, keeping the tip diameter at 3 nm, and base varying at 250, 500, and 1000 nm, the optimal length of the positive region decreases as the base diameter increases [80].

The simulations performed show that conically shaped nanopores featuring a bipolar junction with highly charged positive and negative regions, can indeed offer salt rejection based on electrostatic rejection. The results of the tuning parameters can help shape experimental results as the project progresses, as well as determine the best chemical to modify the pore walls with.

5.4 – Ion Rejection with Track Etched Polymer Membranes

Track etched membranes can be created to model those seen in Figure 5.3. To do so, two types of polymer films were used: polyethylene terephthalate (PET) and polyimide (Kapton 50HN), with a thickness of 12 μm. Membranes obtained from GSI for both PET and Kapton had a pore density of $1x10^8$ pore/cm^2 whereas Kapton membranes purchased from IT4IP had a pore density of $2x10^8$ pores/cm^2. Membranes with a pore density of $\sim10^8$ pores/cm^2 were chosen because 10^9 pores/cm^2 were structurally unstable, and 10^7 pores/cm^2 had no discernable flow.

Creating conical pores for the two types of materials are as follows. For Kapton, etching occurs at 50 ^{o}C at ~13% NaOCl introduced on one side of the foil. The other side of the membrane is in contact with 1M potassium iodide. The side exposed to NaOCl will be the base side. The working electrode is set to 1 V in the NaOCl until the current is 15 μA or 50 minutes has elapsed, whichever comes first. The voltage is then turned off until etch currents reach 200 μA for GSI pores, or 350 μA for IT4IP pores. This process takes between 90-120 minutes. For PET, the etching is done at room temperature. Both sides of the PET membrane are first pre- etched for 15 minutes in 9 M NaOH. The etching solution on the

tip side is then replaced by a stopping solution which consists of 1 M HCOOH and 1 M KCl, while the NaOH remains on the base side. The pre-etching step on the tip side is critical for PET since without it, the membrane does not flow with pressure. Etch currents should reach at least 1 μA , which is generally around 2.5 hours including the pre-etch process.

Current voltage curves for single conically shaped nanopores typically show ion current rectification. When the nanopore system is extrapolated to a multipore membrane containing 10^8 pores/cm^2 however, rectification behavior does not always occur (Figure 5.6). Kapton IV curves feature the asymmetry characteristics to single pores; PET multipore membranes often exhibit an Ohmic behavior, which could be a result of the semi-crystalline structure of PET creating heterogeneous pore openings.

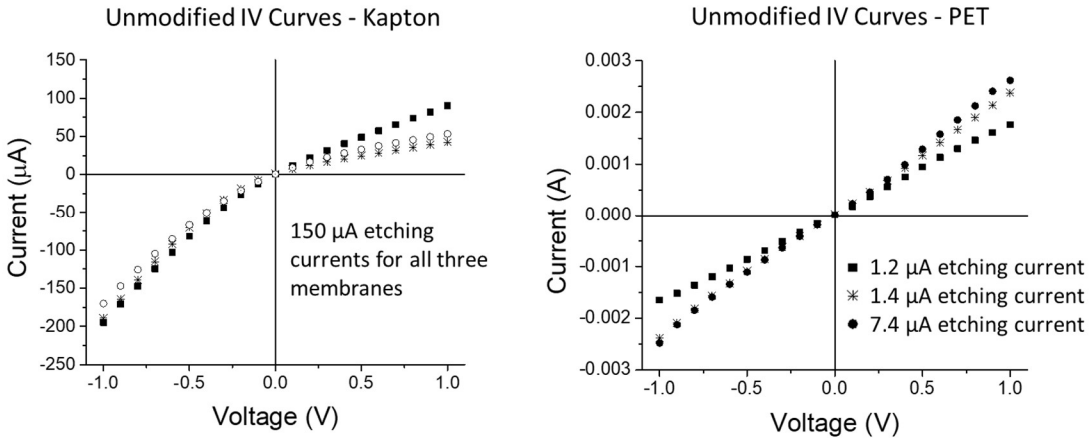

Figure 5.6 – IV curves for three 10^8 pores/cm^2, unmodified Kapton (left) and PET (right) membranes, recorded in 100 mM KCl. The legends indicate the etch currents when the etching process was stopped [80].

I-V curves are also used to size the tip diameter of single conical pores; the base diameter is calculated based on the etching time. For multipore membranes the same approach can be used, however the determined tip opening might be less accurate due to the low resistance of multipore membranes. Consequently, the applied voltage drops not only along the membrane but also in the bulk solution. We tried to mitigate the issue by

placing the electrodes as close to the pore surface as our set-up allowed. An alternate way to determine the base and tip diameters is to image both sides of the membrane. SEM images of the base sides of Kapton and PET membranes show that the base opening is ~600 nm in diameter. The tips were much harder to image. We were more successful in imaging PET pores, due to the pre-etch step; the pores were double-conical in shape that the narrowest part was within the membrane. For Kapton, only tips as large as 30 nm were visible. We believe the smaller openings could have been below the SEM resolution; note that truly single nm resolution might be not be possible for polymer materials due to their roughness. It is also possible that the smallest pores were covered by the conductive material, whose deposition was required for imaging, and not all the pores were etched along the whole length.

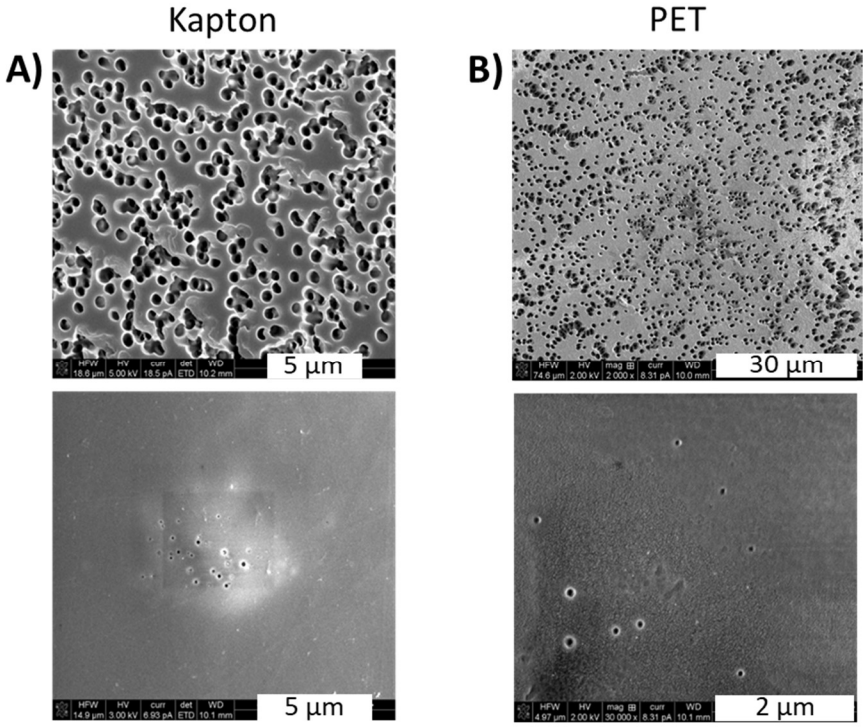

Figure 5.7 – SEM images for **A)** Kapton and **B)** PET membranes. The Kapton membrane has a pore density of 10^8 pores/cm^2 while the PET has a pore density of 10^8 pores/cm^2. The top panels correspond to the base side whereas the bottom panels correspond to tip side. The average base and tip diameters for the imaged Kapton

are 650 and 120 nm respectively, while the average base and tip diameters for the imaged PET are 850 and 100 nm respectively.

Pore diameters based in the I-V curves could be calculated treating the pores as parallel connected resistors. The area exposed to the solution is equivalent of a circle with 1 cm in diameter. For the recordings in 1 M KCl shown for PET membranes in Fig. 5b, the pore opening diameter is ~1 nm.

Pore opening diameter can also be estimated from the Hagen-Pouseuille equation, which describes the pressure drop across a narrow channel, in this case a cone, for an incompressible, Newtonian fluid [82]:

$$Q = \frac{\pi \Delta P}{8 \mu L} r^2 R^2 \tag{5.10}$$

Here, Q is the volumetric flow rate, ΔP is the pressure, μ is the dynamic viscosity of the solution, L is the length of the channel, and r and R are the radii of the tip and base respectively. Typical flow rates for PET and Kapton are ~12 μL/min and ~100 μL/min respectively. Assuming all the pores are open (10^8 per cm^2), the average tip diameter is ~2 nm and 5 nm for PET and Kapton respectively. If the effective pore density was ten times lower, i.e. 10^7 pores/cm^2, giving a tip diameter of ~5 nm and 16 nm for PET and Kapton.

To achieve a bipolar junction membrane, the tip side must be chemically modified to attach positively charged functional groups. The procedure is outlined in Chapter 2 as well as a previous work by Vlassiouk & Siwy [41]. The procedure described attaches ethylenediamine, which gives a single positive charge for every bond formed. However, since the simulations showed that higher salt rejection occurred with higher surface charge density, the modifications were performed with spermine, which doubles the positive charge per bonded group. Figure 5.8 shows example IV curves for both PET and Kapton

membranes with a pore density of 10^8 pores/cm^2. Similar to the unmodified Kapton IV curves, the IV curves for a modified Kapton membrane showed typical curve that is inverted. The IV curve for a modified PET membrane is relatively linear, similar to its unmodified counterpart. The measured ion current for the modified IV curve is generally about half of that seen in the unmodified pore.

The crux of this project is the measurement of the rejection rate, as calculated in Equation 5.9. After etching, the membrane is sandwiched between two Kel-F conductivity cells. The base side faces the high pressure side, which is in contact with the feed solution. The pressure is applied from one of two sources: 1) as air provided from the building, which goes up to 60 psi, and 2) from a scuba tank, which can go to pressures greater than 100 psi. On the tip side, there is a mesh to support the membrane to keep it from tearing and reduce deformations and is open to atmosphere. The permeate is collected in a tared vial and weighed, using the density of water to convert the weighed permeate to a volume. Since the amount of permeate collected is less than 1 mL over several hours, both the feed and permeate are diluted in DI water before conductivity measurements. Typically, 15 µL of the feed and permeate are diluted in 15 mL of DI water. The conductivity of the diluted solution is then measured in a conductivity meter (Fisher Accumet Basic AB30).

As alluded to earlier, stopping the etching process at the proper etch current is quite important. At too large of an etch current, the pore diameters will be too large, decreasing or even eliminating its salt rejection abilities. If the etch current is too small however, the pore may not be large enough to flow. Figure 5.9 showcases this idea, especially the Kapton plot, which highlights the data points in which no flow was observed, whereas the

other data points had flow and a measurable rejection rate. Thus, this becomes an optimization problem to find the etch current with the highest rejection rate.

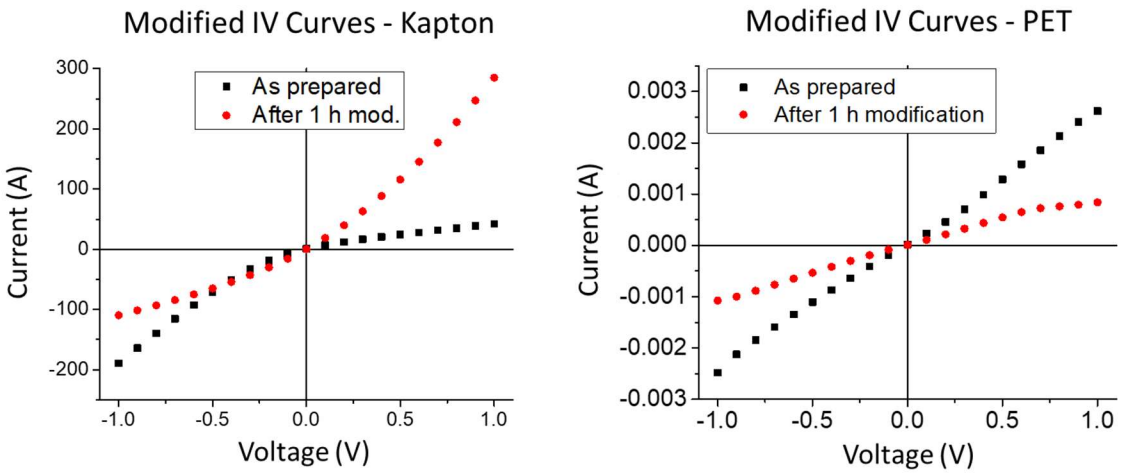

Figure 5.8 – IV curves for 10^8 pores/cm^2 Kapton (left) and PET (right) before and after modifying with spermine. Kapton modification shows an inversed curve compared to the unmodified curve. PET modification shows linear behavior, albeit at a lowered current [80].

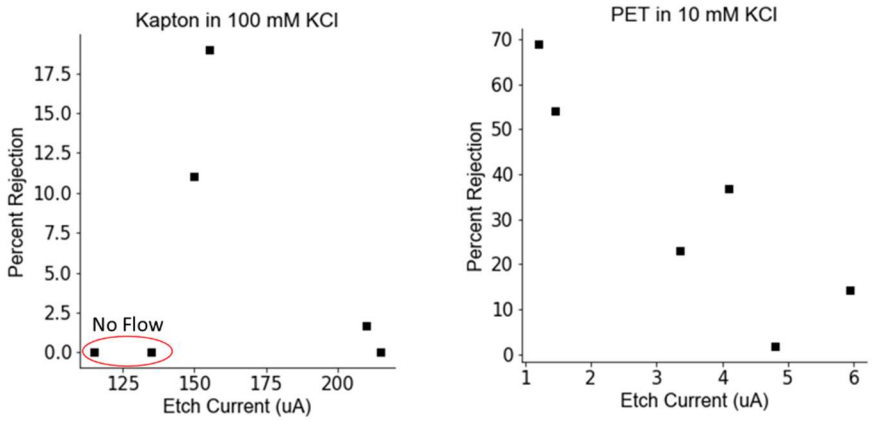

Figure 5.9 – Salt rejection rates for Kapton (left) and PET (right) given their etch currents. The Kapton data points were taken in 100 mM KCl solution, while the PET were in 10 mM KCl solutions. The plots indicate that there is an optimal etch current to reach the highest salt rejection rate. Anything higher will decrease the membranes rejection ability, while anything lower will have no discernable flow.

Table 5.1 shows experimental data points for 8 Kapton pores and 2 PET pores. Whether or not the membrane has been modified is indicated in the middle column. The

last column indicates the percent rejection, as well as the concentration of KCl and pressure the experiment was performed in. Typically, unmodified Kapton membranes in 100 mM KCl have low rejection rates, hovering at ~15%. As predicted by Comsol modelling, the modified Kapton pores have a much higher rejection rate, ranging from 35% to 55% for 100 mM KCl, more than doubling the rejection rate. Membrane 9, made of PET, demonstrates this point further, in that the unmodified pore did not reject salt at all in 100 mM KCl. Post modification however, the salt rejection jumps to 32% under the same experimental conditions. Membrane 3 highlights the concentration effects, in which the rejection rate at 50 KCl higher than the rejection rate at 100 mM KCl; again, this is in agreement with the Comsol modeling.

	Surface Charge	**Percent Rejection**
Membrane 1 – Kapton, 10^8 per cm^2	Diode	35% (100 mM), 60 psi
Membrane 2 - Kapton, 10^8 per cm^2	Diode	41% (100 mM), 60 psi
Membrane 3 - Kapton, 2 10^8 per cm^2	Diode	50% (100 mM), 70 psi; 65% (50 mM), 70 psi
Membrane 4 – Kapton, 10^8 per cm^2	Diode	55% (100 mM), 60 psi
Membrane 5 - Kapton, 10^8 per cm^2	Unmodified	16% (100 mM), 60 psi
Membrane 6 - Kapton, $2 \cdot 10^8$ per cm^2	Unmodified	14% (100 mM), 60 psi
Membrane 7 - Kapton, $2 \cdot 10^8$ per cm^2	Unmodified	14% (100 mM), 60 psi
Membrane 8 – Kapton, 10^8 per cm^2	Unmodified	17% (100 mM), 60 psi
Membrane 9 – PET, 10^8 per cm^2	Unmodified	0% (100 mM), 60 psi
	Diode	32% (100 mM), 60 psi
Membrane 10 - PET, 10^8 per cm^2	Diode	42% (10 mM), 40 psi

Table 5.1 – Experimental data from 10 independent membranes. The membrane material and pore density are indicated in the first column. The 'Surface Charge' column indicates if the data is for a modified or unmodified case. Lastly, the 'Percent Rejection' column indicates the salt rejection measured and its experimental conditions.

Although this work is in its preliminary stages, it is clear that salt rejection occurs in conically shaped polymer pores up to 100 mM KCl solutions. From SEM images and estimates from the Hagen-Poiseuille equation, the tip diameter is estimated to be larger than 3 nm, meaning electrostatic rejection is the dominant mode of separation. The salt rejection is more than doubled if the pore tip is modified with spermine to create bipolar junction. Additional experiments to consider include determining the effects of pressure, solution concentration, and pH. In addition, salt solutions can vary to include other monovalent (i.e. NaCl) and divalent (i.e. $CaCl_2$) salts.

CONCLUSIONS

The thesis has shown a variety of methods to prepare pores with controlled geometry and surface chemistry. These pores were used as a model system to understand transport properties at the nanoscale as well as the basis for preparation of sensors and desalination units.

Polymer pores prepared by the track-etching technique are very versatile and fabrication of conical and cylindrical pores was demonstrated. We showed that pores prepared in polyethylene terephthalate (PET) feature undulating diameters so that they contain zones that are wider and zones which are narrower than the average diameter. This undulating, called also 'rough', pores were found crucial in being able to distinguish between objects that were spherical as well as rod-shaped particles in an experiment called resistive-pulse. We believe this finding extends the current resistive-pulse technique beyond sizing so that multiple physical parameters of individual objects can be determined.

Conically shaped nanopores in PET were prepared as the basis to design a new type of desalination units. Current reverse osmosis membrane reject ions mostly based on size, so that smaller water molecules can pass through, while larger ions are rejected. In order to increase the throughput of desalination, we proposed to use nanopores with diameter as large as 5 nm, containing a junction between positively charged and negatively charged zones on the pore wall. Surface charge density of both zones is high and exceeds 1 elementary charge per nm^2. We demonstrated that ion rejection can indeed be achieved via electric interactions of the passing ions with the charged walls.

Finally, we fabricated single nanopores in a different material, silicon nitride, using a direct electron beam drilling in a transmission electron microscope. These pores equipped

with a gold layer on one surface allowed us to create a nanopore system, whose surface charge properties could be controlled 'contactless' with an electric potential difference applied across the nanopores. This work also demonstrates how gold polarization can be used to induce new ionic properties.

Future work will be directed in combining various pores into ionic circuits to create more complex and versatile nanofluidic systems with application in sensing. Future efforts will also focus on improving homogeneity of the pore opening diameter in multipore membranes to improve their performance in separation processes including desalination.

REFERENCES

[1] C. A. Merchant *et al.*, "DNA Translocation Through Graphene Nanopores," *Nano Lett.*, vol. 10, no. 8, pp. 2915–2921, 2010.

[2] P. Apel, "Track Etching Technique in Membrane Technology," *Radiat. Meas.*, vol. 34, no. 1–6, pp. 559–566, Jun. 2001.

[3] S. Majd, E. C. Yusko, Y. N. Billeh, M. X. Macrae, J. Yang, and M. Mayer, "Applications of Biological Pores in Nanomedicine, Sensing, and Nanoelectronics," *Curr. Opin. Biotechnol.*, vol. 21, no. 4, pp. 439–476, 2010.

[4] Y. Jiang, A. Lee, J. Chen, M. Cadene, B. T. Chait, and R. MacKinnon, "The Open Pore Conformation of Potassium Channels," *Nature*, vol. 417, no. 6888, pp. 523–526, 2002.

[5] B. Zhang *et al.*, "Bench-Top Method for Fabricating Glass-Sealed Nanodisk Electrodes, Glass Nanopore Electrodes, and Glass Nanopore Membranes of Controlled Size," *Anal. Chem.*, vol. 79, no. 13, pp. 4778–4787, 2007.

[6] A. J. Storm, J. H. Chen, X. S. Ling, H. W. Zandbergen, and C. Dekker, "Fabrication of Solid-State Nanopores with Single-Nanometre Precision," *Nat. Mater.*, vol. 2, pp. 537–540, 2003.

[7] C. R. Crick, J. Y. Y. Sze, M. Rosillo-Lopez, C. G. Salzmann, and J. B. Edel, "Selectively Sized Graphene-Based Nanopores for in Situ Single Molecule Sensing," *ACS Appl. Mater. Interfaces*, vol. 7, no. 32, pp. 18188–18194, 2015.

[8] C. C. Harrell, S. B. Lee, and C. R. Martin, "Synthetic Single-Nanopore and Nanotube Membranes," *Anal. Chem.*, vol. 75, no. 24, pp. 6861–6867, 2003.

[9] H. Kwok, K. Briggs, and V. Tabard-Cossa, "Nanopore fabrication by controlled dielectric breakdown," *PLoS One*, vol. 9, no. 3, p. e92880, 2014.

[10] J. J. Kasianowicz, E. Brandin, D. Branton, and D. W. Deamer, "Characterization of individual polynucleotide molecules using a membrane channel," *PNAS*, vol. 93, no. 24, pp. 13770–13773, Nov. 1996.

[11] G. Yellen, "The voltage-gated potassium channels and their relatives," *Nature*, vol. 419, no. 6902, pp. 35–42, 2002.

[12] S. W. Kowalczyk, T. R. Blosser, and C. Dekker, "Biomimetic nanopores: learning from and about nature," *Trends Biotechnol.*, vol. 29, no. 12, pp. 607–614, 2011.

[13] S. Nam, M. J. Rooks, K. Kim, and S. M. Rossnagel, "Ionic Field Effect Transistors with Sub-10 nm Multiple Nanopores," *Nano Lett.*, vol. 9, no. 5, pp. 2044–2048, 2009.

[14] F. Haque, J. Li, H. C. Wu, X. J. Liang, and P. Guo, "Solid-state and biological nanopore for real-time sensing of single chemical and sequencing of DNA," *Nano Today*, vol. 8, no. 1. pp. 56–74, 2013.

[15] A. R. Hall, A. Scott, D. Rotem, K. K. Mehta, H. Bayley, and C. Dekker, "Hybrid pore formation by directed insertion of α-haemolysin into solid-state nanopores," *Nat. Nanotechnol.*, vol. 5, no. 12, pp. 874–877, 2010.

[16] R. L. Fleischer, P. B. Price, and R. M. Walker, "Ion Explosion Spike Mechanism for Formation of Charged-Particle Tracks in Solids," *J. Appl. Phys.*, vol. 36, no. 11, pp. 3645–3652, 1965.

[17] E. C. H. Silk and R. S. Barnes, "Examination of fission fragment tracks with an electron microscope," *Philisophical Mag.*, vol. 4, no. 44, pp. 970–972, 1959.

[18] R. L. Fleischer, P. B. Price, R. M. Walker, and E. L. Hubbard, "Track Registration in Various Solid-State Nuclear Track Detectors," *Phys. Rev.*, vol. 133, no. 5A, pp. A1443–A1450, 1964.

[19] D. A. Young, "Etching of Radiaton Damage in Lithium Fluoride," *Nature*, vol. 182, no. 4632, pp. 375–377, 1958.

[20] B. E. Fischer and R. Spohr, "Production and use of nuclear tracks: Imprinting structure on solids," *Rev. Mod. Phys.*, vol. 55, no. 4, pp. 907–948, 1983.

[21] C. Trautmann, W. Brüchle, R. Spohr, J. Vetter, and N. Angert, "Pore geometry of etched ion tracks in polyimide," *Nucl. Instruments Methods Phys. Res. Sect. B Beam Interact. with Mater. Atoms*, vol. 111, no. 1–2, pp. 70–74, 1996.

[22] G. Szenes, "General features of latent track formation in magnetic insulators irradiated with swift heavy ions," *Phys. Rev. B*, vol. 51, no. 13, pp. 8026–8029, 1995.

[23] R. Katz, "Track Structure Theory in Radiobiology and in Radiation Detection," *Nucl. Track Detect.*, vol. 2, no. 1, pp. 1–28, 1978.

[24] Y. Asakuma, K. Nakagawa, K. Maeda, and K. Fukui, "Theoretical study of the transesterification reaction of polyethylene terephthalate under basic conditions," *Polym. Degrad. Stab.*, vol. 94, no. 2, pp. 240–245, 2009.

[25] R. L. Fleischer, P. B. Price, and R. M. Walker, *Nuclear Tracks in Solids: Principles and Applications*. Berkeley, CA: University of California Press, 1975.

[26] H. G. Paretzke, T. A. Gruhn, and E. V Benton, "The Etching of Polycarbonate Charged Particle Detectors by Aqueous Sodium Hydroxide," *Nucl. Instruments Methods*, vol. 107, no. 3, pp. 597–600, 1973.

[27] P. Y. Apel, Y. E. Korchev, Z. Siwy, R. Spohr, and M. Yoshida, "Diode-like single-ion track membrane prepared by electro-stopping," *Nucl. Instruments Methods Phys. Res. Sect. B Beam Interact. with Mater. Atoms*, vol. 184, no. 3, pp. 337–346, 2001.

[28] C. Chad Harrell, Z. S. Siwy, and C. R. Martin, "Conical Nanopore Membranes: Controlling the Nanopore Shape," *Small*, vol. 2, no. 2, pp. 194–198, 2006.

[29] Z. Siwy and A. Fuliński, "Fabrication of a Synthetic Nanopore Ion Pump," *Phys. Rev. Lett.*, vol. 89, no. 19, p. 198103, 2002.

[30] M. Y. Wu, D. Krapf, M. Zandbergen, H. Zandbergen, and P. E. Batson, "Formation of nanopores in a SiN/SiO_2 membrane with an electron beam," *Appl. Phys. Lett.*, vol. 87, no. 11, pp. 1–4, 2005.

[31] G. S. Chen, C. B. Boothroyd, and C. J. Humphreys, "Electron-beam-induced damage in amorphous SiO_2 and the direct fabrication of silicon nanostructures," *Philos. Mag. A*, vol. 78, no. 2, pp. 491–506, 1998.

[32] M. J. Kim, B. McNally, K. Murata, and A. Meller, "Characteristics of solid-state nanometre pores fabricated using a transmission electron microscope," *Nanotechnology*, vol. 18, no. 20, p. 205302, 2007.

[33] Z. Siwy, D. Dobrev, R. Neumann, C. Trautmann, and K. Voss, "Methods of Producing Nanostructures in Membranes and Asymmetrical Membranes," US patent 20030159985, 2003.

[34] P. Y. Apel, I. V. Blonskaya, S. N. Dmitriev, O. L. Orelovitch, A. Presz, and B. A. Sartowska, "Fabrication of nanopores in polymer foils with surfactant-controlled longitudinal profiles," *Nanotechnology*, vol. 18, no. 30, p. 305302, 2007.

[35] L. M. Innes *et al.*, "Velocity profiles in pores with undulating opening diameter and their importance for resistive-pulse experiments," *Anal. Chem.*, vol. 86, no. 20, pp. 10445–10453, 2014.

[36] R. B. Schoch, J. Han, and P. Renaud, "Transport phenomena in nanofluidics," *Rev. Mod. Phys.*, vol. 80, no. 3, pp. 839–883, 2008.

[37] H. Daiguji, P. Yang, and A. Majumdar, "Ion Transport in Nanofluidic Channels," *Nano Lett.*, vol. 4, no. 1, pp. 137–142, 2004.

[38] R. F. Probstein, *Physicochemical Hydrodynamics*, 2nd ed. New York, NY: John Wiley & Sons, INC., 1994.

[39] M. R. Powell, I. Vlassiouk, C. Martens, and Z. S. Siwy, "Nonequilibrium 1/f Noise in Rectifying Nanopores," *Phys. Rev. Lett.*, vol. 103, no. 24, p. 248104, 2009.

[40] G. Nguyen, I. Vlassiouk, and Z. S. Siwy, "Comparison of bipolar and unipolar ionic diodes," *Nanotechnology*, vol. 21, no. 26, pp. 1–8, 2010.

[41] I. Vlassiouk and Z. S. Siwy, "Nanofluidic diode," *Nano Lett.*, vol. 7, no. 3, pp. 552–556, 2007.

[42] S. Qian and Y. Ai, *Electrokinetic Particle Transport in Micro-/Nanofluidics: Direct Numerical Simulation Analysis*. Boca Raton, Fl: CRC Press, 2012.

[43] M. Firnkes, D. Pedone, J. Knezevic, M. Döblinger, and U. Rant, "Electrically facilitated translocations of proteins through silicon nitride nanopores: Conjoint and competitive action of diffusion, electrophoresis, and electroosmosis," *Nano Lett.*, vol. 10, no. 6, pp. 2162–2167, 2010.

[44] W. H. Coulter, "Means for counting particles suspended in a fluid," US Patent 2,656,508, 1953.

[45] R. W. DeBlois and C. P. Bean, "Counting and Sizing of Submicron Particles by the Resistive Pulse Technique," *Rev. Sci. Instrum.*, vol. 41, no. 7, pp. 909–916, 1970.

[46] M. Pevarnik, K. Healy, M. E. Toimil-Molares, A. Morrison, S. E. Létant, and Z. S. Siwy, "Polystyrene Particles Reveal Pore Substructure As They Translocate," *ACS Nano*, vol. 6, no. 8, pp. 7295–302, Aug. 2012.

[47] D. C. Golibersuch, "Observation of Aspherical Particle Rotation in Poiseuille Flow via the Resistance Pulse Technique I. Application to Human Erythrocytes," *Biophys. J.*, vol. 13, pp. 265–280, 1973.

[48] A. Kuijk, A. van Blaaderen, and A. Imhof, "Synthesis of Monodisperse, Rodlike Silica Colloids with Tunable Aspect Ratio," *J. Am. Chem. Soc.*, vol. 133, no. 8, pp. 2346–2349, 2011.

[49] Y. Qiu *et al.*, "Pores with Longitudinal Irregularities Distinguish Objects by Shape," *ACS Nano*, vol. 9, no. 4, pp. 4390–4397, 2015.

[50] W. J. Lan, C. Kubeil, J. W. Xiong, A. Bund, and H. S. White, "Effect of Surface Charge on the Resistive Pulse Waveshape during Particle Translocation through Glass Nanopores," *J. Phys. Chem. C*, vol. 118, no. 5, pp. 2726–2734, 2014.

[51] J. Menestrina, C. Yang, M. Schiel, I. Vlassiouk, and Z. S. Siwy, "Charged Particles Modulate Local Ionic Concentrations and Cause Formation of Positive Peaks in Resistive-Pulse-Based Detection," *J. Phys. Chem. C*, vol. 118, no. 5, pp. 2391–2398, Feb. 2014.

[52] J. A. Osborn, "Demagnetizing Factors of the General Ellipsoid," *Phys. Rev.*, vol. 67, no. 11–12, pp. 351–357, 1945.

[53] M. M. Tirado and J. G. de la Torre, “Rotational dynamics of rigid, symmetric top macromolecules. Application to circular cylinders,” *J. Chem. Phys.*, vol. 73, no. 4, pp. 1986–1993, 1980.

[54] S. Müller *et al.*, “Electrochemical Synthesis of $Bi_{1-x}Sb_x$ Nanowires with Simultaneous Control on Size, Composition, and Surface Roughness,” *Cryst. Growth Des.*, vol. 12, no. 2, pp. 615–621, 2011.

[55] R. Karnik, C. Duan, K. Castelino, H. Daiguji, and A. Majumdar, “Rectification of Ionic Current in a Nanofluidic Diode,” *Nano Lett.*, vol. 7, no. 3, pp. 547–551, 2007.

[56] M. E. Gracheva, D. V. Melnikov, and J. P. Leburton, “Multilayered Semiconductor Membranes for Nanopore Ionic Conductance Modulation,” *ACS Nano*, vol. 2, no. 11, pp. 2349–2355, 2008.

[57] W. Guan, R. Fan, and M. A. Reed, “Field-effect reconfigurable nanofluidic ionic diodes,” *Nat. Commun.*, vol. 2, no. 1, p. 506, 2011.

[58] J.-F. Pietschmann *et al.*, “Rectification properties of conically shaped nanopores: consequences of miniaturization,” *Phys. Chem. Chem. Phys.*, vol. 15, no. 39, pp. 16917--16926, 2013.

[59] M. Nishizawa, V. P. Menon, and C. R. Martin, “Metal Nanotubule Membranes with Electrochemically Switchable Ion-Transport Selectivity,” *Science*, vol. 268, no. 5211, pp. 700–702, 1995.

[60] C. Yang, P. Hinkle, J. Menestrina, I. V. Vlassiouk, and Z. S. Siwy, “Polarization of Gold in Nanopores Leads to Ion Current Rectification,” *J. Phys. Chem. Lett.*, vol. 7, no. 20, pp. 4152–4158, 2016.

[61] T. M. Squires and M. Z. Bazant, “Induced-charge electro-osmosis,” *J. Fluid Mech.*, vol. 509, pp. 217–252, Jun. 2004.

[62] A. J. Pascall and T. M. Squires, “Induced Charge Electro-osmosis over Controllably Contaminated Electrodes,” *Phys. Rev. Lett.*, vol. 104, no. 8, p. 88301, Feb. 2010.

[63] J. E. Hall, “Access Resistance of a Small Circular Pore,” *J. Gen. Physiol.*, vol. 66, no. 4, pp. 531–532, 1975.

[64] H. A. Asiri and A. B. Anderson, “Mechanisms for Ethanol Electrooxidation on Pt(111) and Adsorption Bond Strengths Defining an Ideal Catalyst,” *J. Electrochem. Soc.*, vol. 162, no. 1, pp. F115–F122, 2015.

[65] G. Tremiliosi-Filho, E. R. Gonzalez, A. J. Motheo, E. M. Belgsir, J. M. Léger, and C. Lamy, “Electro-oxidation of ethanol on gold: Analysis of the reaction products and mechanism,” *J. Electroanal. Chem.*, vol. 444, no. 1, pp. 31–39, 1998.

[66] Y. P. Liu *et al.*, "Electrooxidation of Ethanol and Methanol Using the Molecular Catalyst [{$Ru_4O_4(OH)_2(H_2O)_4$}(γ-$SiW_{10}O_{36})_2$]$^{10-}$," *J. Am. Chem. Soc.*, vol. 138, no. 8, pp. 2617–2628, 2016.

[67] J. Cervera, A. Alcaraz, B. Schiedt, R. Neumann, and P. Ramírez, "Asymmetric Selectivity of Synthetic Conical Nanopores Probed by Reversal Potential Measurements," *J. Phys. Chem. C*, vol. 111, no. 33, pp. 12265–12273, 2007.

[68] T. Gamble, E. Gillette, S. B. Lee, and Z. S. Siwy, "Probing Porous Structure of Single Manganese Oxide Mesorods with Ionic Current," *J. Phys. Chem. C*, vol. 117, no. 47, pp. 24836–24842, 2013.

[69] Z. S. Siwy, "Ion-current rectification in nanopores and nanotubes with broken symmetry," *Adv. Funct. Mater.*, vol. 16, no. 6, pp. 735–746, 2006.

[70] J. G. Wijmans and R. W. Baker, "The solution-diffusion model: a review," *J. Memb. Sci.*, vol. 107, no. 1–2, pp. 1–21, 1995.

[71] U. Merten, *Desalination by reverse osmosis*. Cambridge, MA: M.I.T. Press, 1966.

[72] T.-M. Chang and L. X. Dang, "Detailed Study of Potassium Solvation Using Molecular Dynamics Techniques," *J. Phys. Chem. B*, vol. 103, no. 22, pp. 4714–4720, 1999.

[73] S. J. Stuart and B. J. Berne, "Effects of Polarizability on the Hydration of the Chloride Ion," *J. Phys. Chem.*, vol. 100, no. 29, pp. 11934–11943, 1996.

[74] A. Yaroshchuk, Y. Boiko, and A. Makovetskiy, "Ion-rejection, Electrokinetic and Electrochemical Properties of a Nanoporous Track-Etched Membrane and Their Interpretation by Means of Space Charge Model," *Langmuir*, vol. 25, no. 16, pp. 9605–9614, 2009.

[75] A. Szymczyk and H. Zhu, "Ion Rejection Properties of Nanopores with Bipolar Fixed Charge Distributions," *J. Phys. Chem. B*, vol. 114, no. 31, pp. 10143–10150, 2010.

[76] A. P. Thompson, "Nonequilibrium molecular dynamics simulation of electro-osmotic flow in a charged nanopore," *J. Chem. Phys.*, vol. 119, no. 14, pp. 7503–7511, 2003.

[77] J. Goldsmith and C. C. Martens, "Pressure-induced water flow through model nanopores," *Phys. Chem. Chem. Phys.*, vol. 11, no. 3, pp. 528–533, 2009.

[78] A. Szymczyk, H. Zhu, and B. Balannec, "Pressure-Driven Ionic Transport through Nanochannels with Inhomogenous Charge Distributions," *Langmuir*, vol. 26, no. 2, pp. 1214–1220, 2010.

[79] A. Santafé-Moros and J. M. Gozálvez-Zafrilla, "Nanofiltration Modeling Based on the Extended Nernst-Planck Equation under Different Physical Modes," in *Proceedings of*

the COMSOL Conference 2008, Hannover, Germany, 2008.

[80] Z. S. Siwy, Y. Qiu, C. Yang, and J. Boyd, "Desalination Beyond Debye Screening Length Using Highly Charged Membranes with Asymmetric Nanopores," US Record of Invention Disclosure, 2017.

[81] *Reverse Osmosis and Nanofiltration - Manual of Water Supply Practices, M46*, 2nd ed. American Water Works Association, 2007.

[82] E. B. Kalman, "Controlling Ionic Transport for Device Design in Synthetic Nanopores," University of California, Irvine, 2010.